

Alma Mater Studiorum Università di Bologna  
Archivio istituzionale della ricerca

Drainage of a deep magma reservoir near Mayotte inferred from seismicity and deformation

This is the final peer-reviewed author's accepted manuscript (postprint) of the following publication:

*Published Version:*

Cesca S., Letort J., Razafindrakoto H.N.T., Heimann S., Rivalta E., Isken M.P., et al. (2020). Drainage of a deep magma reservoir near Mayotte inferred from seismicity and deformation. NATURE GEOSCIENCE, 13(1), 87-93 [10.1038/s41561-019-0505-5].

*Availability:*

This version is available at: <https://hdl.handle.net/11585/775282> since: 2020-10-20

*Published:*

DOI: <http://doi.org/10.1038/s41561-019-0505-5>

*Terms of use:*

Some rights reserved. The terms and conditions for the reuse of this version of the manuscript are specified in the publishing policy. For all terms of use and more information see the publisher's website.

This item was downloaded from IRIS Università di Bologna (<https://cris.unibo.it/>).  
When citing, please refer to the published version.

(Article begins on next page)

This is the final peer-reviewed accepted manuscript of:

Cesca, S., Letort, J., Razafindrakoto, H. N. T., Heimann, S., Rivalta, E., Isken, M. P., Nikkhoo, M., Passarelli, L., Petersen, G., Cotton, F., Dahm, T. (2020): Drainage of a deep magma reservoir near Mayotte inferred from seismicity and deformation. – Nature Geoscience, 13, 87-93.

The final published version is available online at: <https://doi.org/10.1038/s41561-019-0505-5>

#### Rights / License:

The terms and conditions for the reuse of this version of the manuscript are specified in the publishing policy. For all terms of use and more information see the publisher's website.

*This item was downloaded from IRIS Università di Bologna (<https://cris.unibo.it/>)*

***When citing, please refer to the published version.***

# **Drainage of a deep magma reservoir near Mayotte inferred from seismicity and deformation**

Simone Cesca<sup>1,\*</sup>, Jean Letort<sup>2</sup>, Hoby N. T. Razafindrakoto<sup>1</sup>, Sebastian Heimann<sup>1</sup>, Eleonora Rivalta<sup>1</sup>,  
Marius P. Isken<sup>3</sup>, Mehdi Nikkhoo<sup>1</sup>, Luigi Passarelli<sup>4</sup>, Gesa M. Petersen<sup>1,5</sup>, Fabrice Cotton<sup>1,5</sup> &  
Torsten Dahm<sup>1,5</sup>

<sup>1</sup> GFZ German Research Centre for Geosciences, Potsdam, Germany

<sup>2</sup> IRAP - Observatoire Midi Pyrénées, Toulouse, France

<sup>3</sup> University of Kiel, Germany

<sup>4</sup> King Abdullah University of Science and Technology (KAUST), Thuwal, Saudi Arabia

<sup>5</sup> University of Potsdam, Germany

\* corresponding author [simone.cesca@gfz-potsdam.de](mailto:simone.cesca@gfz-potsdam.de)

The dynamics of magma deep in the Earth's crust are difficult to capture by geophysical monitoring. Since May 2018, a seismically quiet area offshore of Mayotte, in the Comoros archipelago, has been affected by a complex seismic sequence, including long-duration, very long period signals recorded globally. A large surface deflation has also been recorded by GNSS stations on Mayotte. Here we systematically analyse regional and global seismic and deformation data to provide a one year long detailed picture of a deep, rare magmatic process. We identify about 7000 volcano-tectonic earthquakes and 407 very long period signals. Early earthquakes migrated upward in response to a magmatic dyke propagating from Moho depth to the surface, while later events marked the progressive failure of the roof of a magma reservoir, triggering its resonance. An analysis of the very long period seismicity and deformation suggests that a 25-35 km deep reservoir of 10-15 km diameter has lost at least 1.3 km<sup>3</sup> of magma. We demonstrate that such deep offshore magmatic activity can be captured without any on-site monitoring.

In May-June 2018, global earthquake monitoring agencies detected a series of large earthquakes in an otherwise relatively quiet area ~35 km east of the island of Mayotte. A peak  $M_w$  5.9<sup>1</sup> earthquake occurred on 15 May 2018, the largest ever recorded in the region. In November 2018 long-duration (~20 minutes) very long period seismic signals (VLPs) with periods of ~16 s were discovered in global seismic recordings<sup>1</sup>, triggering the curiosity of the scientific community. The origin of the VLPs was traced back in the vicinity of the swarm activity close to Mayotte. Most often, VLP signals<sup>2</sup> are recorded in volcanic areas<sup>3</sup> suggesting a magmatic origin for the sequence.

Mayotte is one of the four principal volcanic islands in the Comoros archipelago and home to a population of ~256,000 (2017). The island belongs to a 250 km long NW-SE chain of basaltic volcanoes located between Africa and Madagascar (Fig. 1). The region has been affected by multiple tectonic processes<sup>4,5</sup> including an episode of NE-SW trend rifting during the Permo-Triassic, associated with the fragmentation of Gondwana<sup>6,7</sup> and the formation of the Somali and Mozambique oceanic basins, during which Madagascar drifted southwards<sup>8-12</sup>. Proposed sources of volcanism include hotspot<sup>13</sup>, passive magma ascent through lithospheric discontinuities<sup>14</sup> or rifting coeval to rifting in Southern East Africa<sup>15</sup>. Volcanism at Mayotte started at about 10-20 Ma<sup>15-16</sup> and subsequently migrated to produce the other islands. Mayotte last erupted 4000±500 years ago<sup>15</sup>. The nature of the crust and its thickness beneath the Comoro Islands is debated<sup>14-15</sup>. Only a few  $M > 4$  earthquakes have been recorded in this area, including the 1993 Mb 5.2 event, which caused ~1.7 M Euros of damage in Mayotte, and the 2011 Mb 4.9<sup>16</sup>. Focal mechanisms and GNSS data support NE-SW transtension<sup>17-18</sup>.

By modeling seismological data at regional and teleseismic distances and ground displacement recordings at Mayotte (Fig. S1) collected between May 2018 and April 2019, we provide evidence of the drainage of  $1.7 \pm 0.4 \text{ km}^3$  of magma from a ~30 km deep sub-Moho magma reservoir by a

dyke that propagated to the seafloor. The dyke propagation caused a swarm of almost 7000 volcano-tectonic earthquakes (VTs) and the downsag of the host rock overlying the reservoir, which in turn triggered its resonance, emitting 407 long-duration VLPs, and helped sustain a high outflow rate throughout. We argue that reservoir roof failures at calderas, which are well-studied, can be used as a down-scaled analogue to evaluate future scenarios.

## **Data analysis and modeling**

We use seismic data at regional and teleseismic distances (ABKAR seismic array, Kazakhstan) and test different velocity models (Fig. S2, Tables S1-S4) to perform full waveform moment tensor (MT) inversions and depth phase analysis, thereby retrieving focal mechanisms, centroid locations (Figs. S3-S5) and depths (Figs. S6-S8) for the most energetic VTs<sup>19</sup>. Additionally, we take advantage of seismic station YTMZ, deployed over the full study period on Mayotte, to produce an enhanced catalogue<sup>19</sup> of relative locations of weaker VTs (Fig. S9). We detect 6990 VTs and locate 1904 of them (Fig. 1) by retrieving their origin direction and distance (Figs. S10-S11; see Supplementary Information, SI). The VTs are classified into families of events (colour-coded in Figs. 1 and 2a-c) with similar waveforms and distance to station YTMZ (Fig. S12). We design a detection tool to scan the broadband data at four regional seismic stations for monochromatic, low-frequency signals, thereby detecting 407 long-duration VLPs<sup>19</sup> (Fig. S13). We also develop an algorithm to invert for the centroid MT of the VLPs and resolve the damping constant and dominant frequency of a damped linear oscillator as the source time function, obtaining high-quality solutions for 22 VLPs<sup>19</sup> (Fig. 3). Due to the uncertainties on Moho depth and crustal structure, all our results are tested against different velocity models with varying Moho depth (SI).

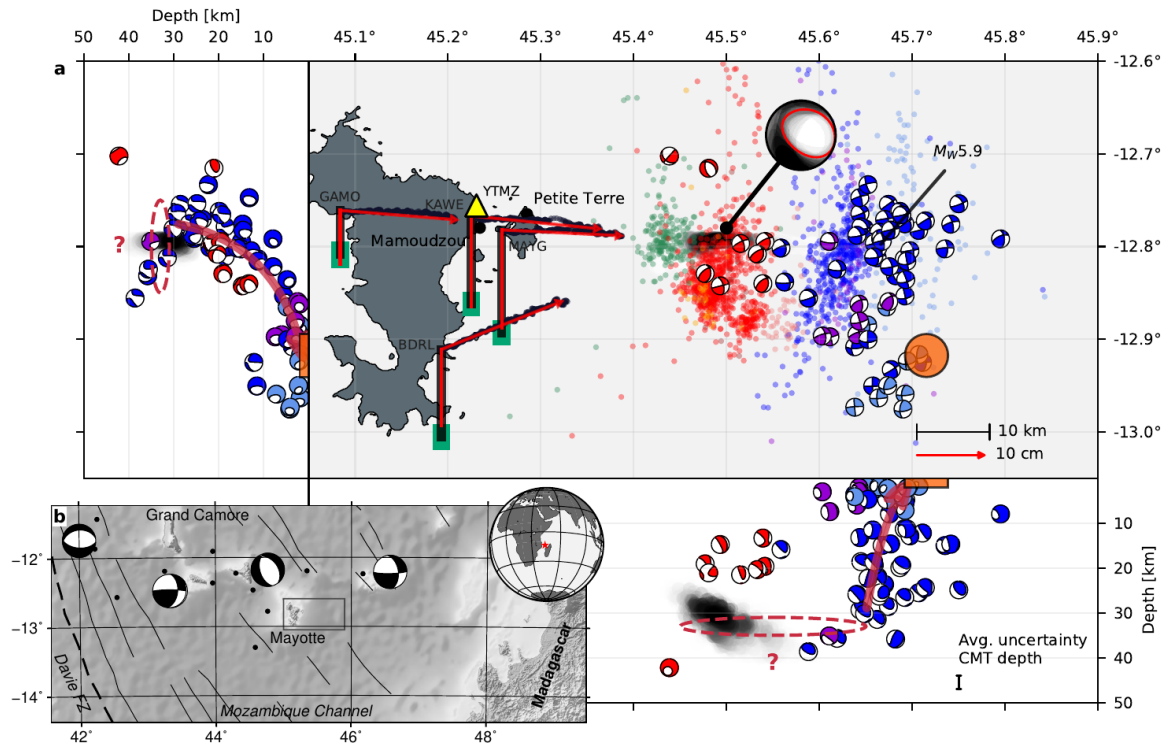


**Fig. 1 | Map view and cross sections of seismic and deformation sources. a,** Weak VT locations (points) and strong VT MTs (focal sphere, lower hemisphere projections of the double-couple components in map view and backprojection of full MTs from East or South in the cross sections, respectively) plotted colour-coded according to similarity of waveform and distance to station YTMZ (yellow triangle), overlay of 22 VLPs MTs (black focal spheres, negative CLVD convention used), best-fit point deformation sources (black symbols, SI), vertical displacements (black lines) and time evolution of horizontal displacements at four GNSS stations (black scatter points, 1 July, 2018 to 1 April, 2019), uncertainties within  $2\sigma$  of vertical displacements (green boxes, horizontal uncertainties negligible with respect to vertical ones), best fitting modelled displacements (red lines and arrows) and the inferred VLP source location (dashed red ellipses). The south-east and upward migration paths of seismicity and magma in Phases I-II (dashed black arrows in the cross-sections) reach the location of the discovered seamount<sup>20</sup> (orange circle and bars, assuming a 5 km diameter<sup>20</sup>). **b,** Map of the Comoro Islands, major regional tectonic structures and basin configuration<sup>5</sup>, showing fracture zones (thin lines) and earthquake locations and MTs prior to the sequence (circle and focal spheres, source GlobalCMT, GEOFON and USGS catalogues); shaded-

relief topography and bathymetry from the ETOPO1 Global Relief Model from NOAA's National Centers for Environmental Information. The location of the study region is highlighted by a red star on the Earth globe.

### **Chronology of the crisis**

We have identified four phases of the volcano-seismic crisis. During Phase I (10 May – 7 June 2018) the most energetic VT burst of the sequence (11  $M_w > 5$  events between 15 and 20 May) occurred ~35 km East of Mayotte (Fig. 2a). We find a depth of 22 km for the largest  $M_w$  5.9 earthquake. Between 31 May – 7 June 2018, the seismicity migrated upward, as confirmed by the centroid depth estimations and array beam analysis (Figs. 2c, S7-S8). During Phase II (7 June – 18 June 2018) epicenters migrated Southwards approaching the recently discovered seamount<sup>20</sup> (Figs. 1, S5). Left-lateral strike-slip faulting dominates in Phases I-II (Fig. 1). A consistent expansion-related isotropic component, increasing gradually up to 20% of the total moment, is found during the upward migration and in Phase II (Figs. S5-S6). By mid June, a new type of activity emerged in the form of long-duration VLPs. However, early VLPs had already occurred on 30 January and 2 June.

Few  $M_w > 4.5$  VTs (Fig. 2a) occurred in Phase III (28 June – 17 September 2018), while VLPs became dominant. Phase IV (17 September, 2018 – March 2019) started with an increasing VLP rate, this time accompanied by a new type of VTs (Fig. 2c,d). The dominant period of VLPs increased smoothly from ~15.2 s (June 2018) to a maximum of ~15.6 s (October 2018), before decreasing again to ~15.3 s (February 2019; Fig. 2e, S13).



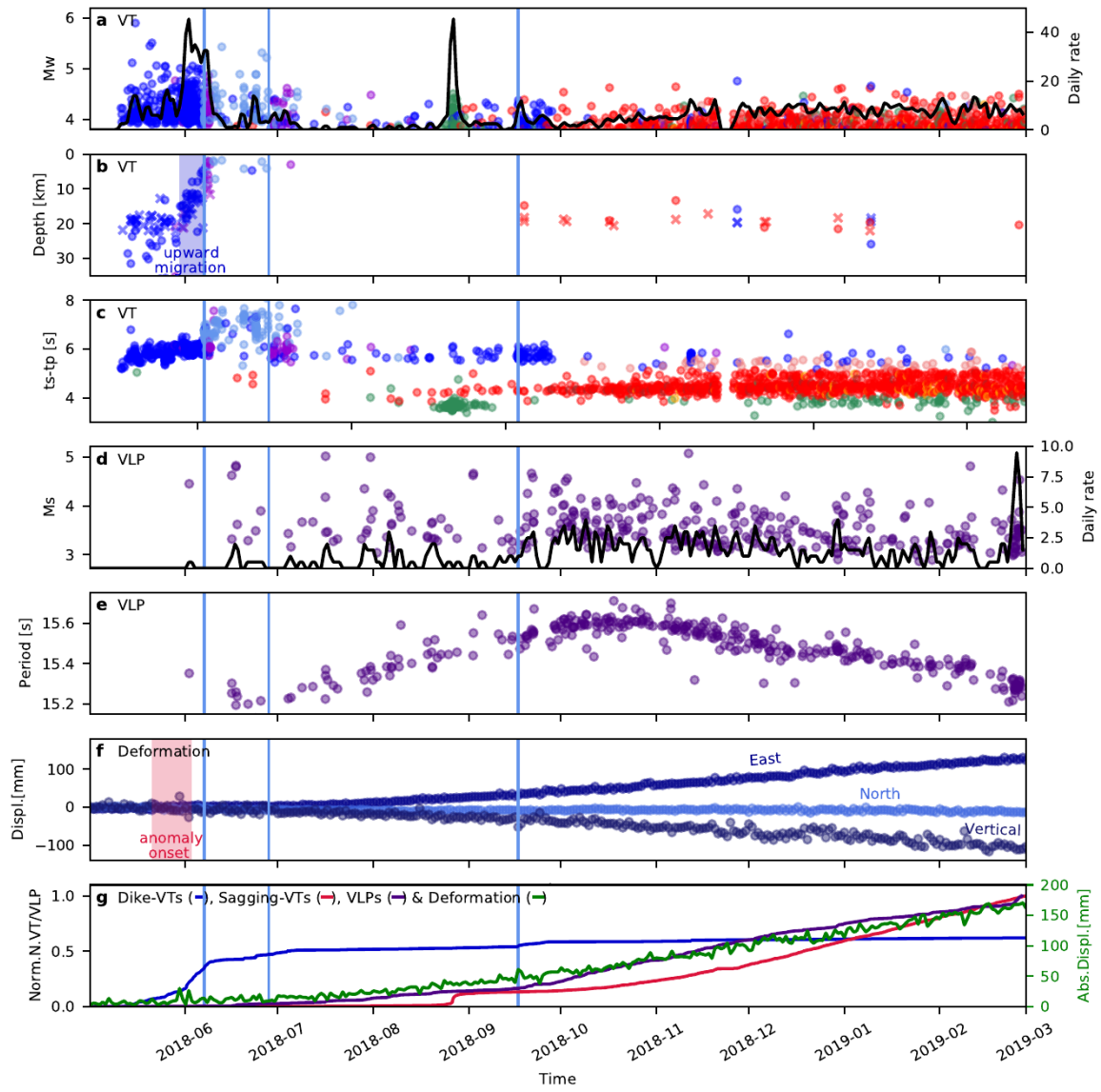


**Fig. 2 | Timeline of the seismic sequence.** **a**, VT magnitudes (colour-coding as in Fig. 1) and seismicity rate (black line); **b**, VT depth based on MT inversion (circles) and array analysis (crosses); **c**, Differential S-P time of VTs at station YTMZ as a proxy of the distance to Mayotte (see SI for uncertainties); **d**, VLP magnitudes ( $M_s$ , purple circles) and rate (black line); **e**, VLP dominant periods (purple circles); **f**, Demeaned and detrended East, North, and vertical GNSS displacements at station MAYG; **g**, Normalized cumulative number of dyke-related VTs (blue line refers to blue, cyan and purple VTs in panels a-c), sagging-related VTs (red line refers to red and green VTs in panels a-c), VLPs (indigo line) and length of GNSS displacement vectors at station MAYG (green line). Sequence phases are marked in all panels with cyan vertical bars.

The VLP MTs are similar (Fig. 1), with a predominance of alternating positive and negative vertical Compensated Linear Vector Dipole (CLVD) (Fig. 3). The vertically axisymmetric MTs suggest a subhorizontal crack, dipping slightly to the West. Centroid locations are the same within errors and depths are at  $37 \pm 11$  km. The largest VLP occurred on 11 November, 2018, with an estimated surface wave magnitude of  $M_s$  5.1. The damping of the VLP source (quality factor,  $Q$ ) is in the range  $72 \pm 6$ , which is higher than in other cases<sup>21-22</sup> but not unique<sup>23</sup>. VLPs onsets are often quasi-simultaneous to one or multiple weak VTs, as observed previously<sup>23</sup>. Due to the emergent nature of VLP signals, it is difficult to judge whether VTs precede or follow VLPs, but some VLPs respond to VTs with abrupt signal amplitude changes, depending on whether the successive VTs are in or out of phase with the resonating VLP source (Fig. 4a). This observation suggests that VTs act as repeated forcing, contributing to the exceptionally long duration of some VLPs. The VLP spectra (Fig. 4b) reveal higher modes including non-integer ratios between them.

All VTs accompanying VLPs and most VTs in Phases III–IV (red and green dots, Figs. 1 and 2a,c) are located closer to Mayotte and have steep NE-SW striking thrust mechanisms (Fig. 1), inconsistent with local transtension. An isolated burst of VTs at the end of August 2018 included earthquake repeaters and anti-repeaters, with highly correlated and anti-correlated waveforms, respectively (Fig. 4c). VTs and VLPs have persisted throughout Phase IV until the time of writing. The cumulative moment of VTs in Phases III-IV is  $M_0 = 5.42 \cdot 10^{16}$  Nm, corresponding to  $M_w = 5.1$ , far less than for the dyke-related seismicity in Phases I-II ( $M_0 = 2.03 \cdot 10^{18}$  Nm,  $M_w = 6.2$ ).

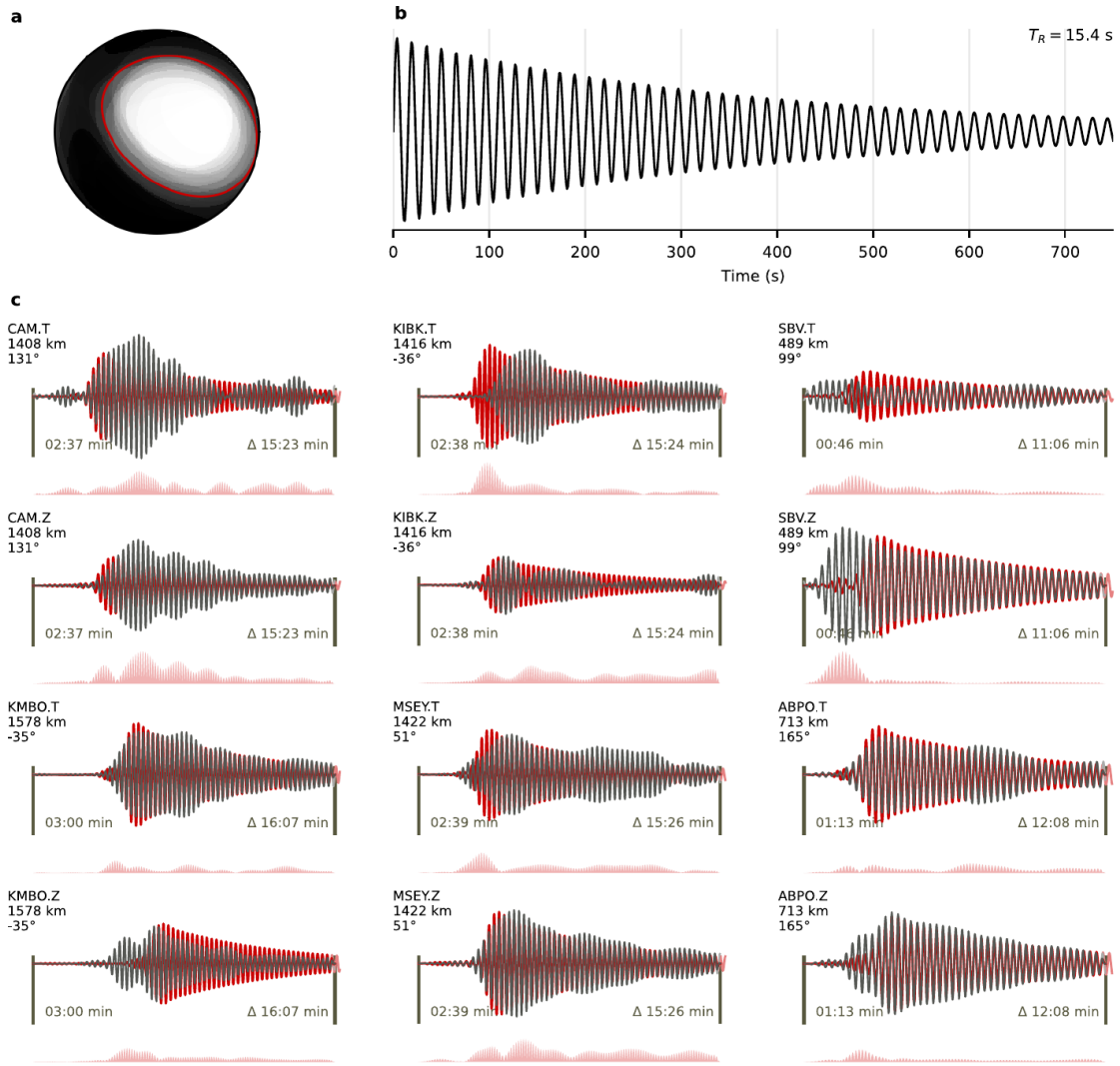


**Fig. 3 | MT solution for the 31 July, 2018 VLP. a,** The MT plot overlays the focal spheres of the ensemble of bootstrap solutions (SI). The red line denotes the overall best solution. The negative CLVD convention is applied. **b,** The resolved, oscillating source time function, with a dominant period  $T_R = 15.4$  s . **c,** Comparison of observed (red lines) and synthetic displacement traces (black lines), as well as their differences (red areas) for a selection of stations and components. Synthetic traces were computed assuming a continental (model P2017, see SI) or oceanic crust, based on station locations (Station name, spatial component, epicentral distance, azimuth, time window starting time, respect to the origin time, and time window duration are reported for each subplot).

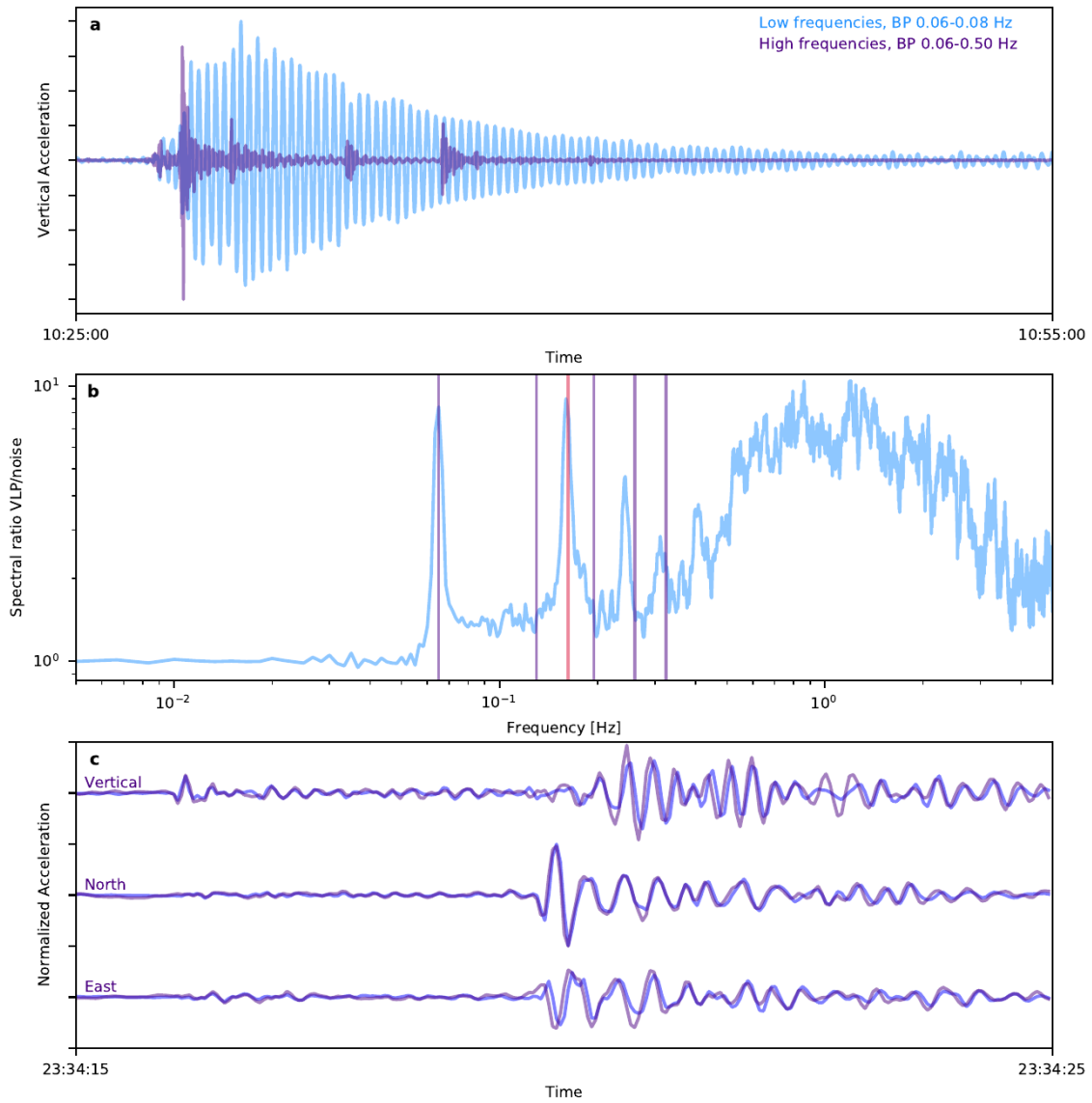


**Fig. 4 | Example of seismic signals and spectra recorded at the YTMZ station. a**, 11 November, 2018 VLP. Waveforms correspond to normalized vertical acceleration filtered in different frequency bands; **b**, Stack of normalized vertical spectra for 51 VLPs (indigo bars represent integer multiples of the dominant frequency (0.065 Hz, or 15.4 s) with a red bar for the 2.5 multiple) **c**, anti-correlated waveforms for two VTs occurring 1.5 min apart on 20 August 2018 (time windows starting at 21:34:15.5 and 21:35:39.6 respectively). Waveforms of the first event (indigo) are compared to flipped waveforms of the second event (blue).

Geodetic data from Mayotte Island reveal a steady, long-lasting subsidence and eastward displacement at four GNSS stations. The length of the displacement vector from July 2018 through April 2019 is 18 cm. Early ground deformation is weak, and grows clearly from July onward. We constrain the location, depth, aspect ratio and volume change by inverting these GNSS data for the time interval 1 July, 2018 - 31 March, 2019. An isotropic source of pressure is unable to simultaneously fit the ratio of horizontal to vertical displacement and the vectors' orientation<sup>1</sup>. We use generalised point-source deformation models<sup>24-25</sup>, first assuming a vertical ellipsoidal source<sup>26</sup> and investigating the effect of layering on the inferred source shape (Figs. S14-S15). The best fit is given by a large negative isotropic plus a small positive vertical CLVD source 12±4 km East of Petit Terre at a depth of 32±3 km, volume change is here -1.7±0.4 km<sup>3</sup>. We also test non-axisymmetric generalised point sources in a homogenous medium<sup>24</sup>, obtaining a laterally contracting vertical dislocation as the best-fit deformation mechanism at a depth of 23 km and expelled magma volume (potency) of -1.3 km<sup>3</sup> with 99% confidence bounds of (20, 27) km and (-2.8, -1.2) km<sup>3</sup>, respectively. This is a lower bound of the source potency since all GNSS stations are grouped on one side of the source, so that the network has no sensitivity to NS source contraction. Both analyses indicate that vertical shrinking of the source is negligible, suggesting that the shrinking source does not coincide with the source of the VLPs.

### **Interpretation of chain of events**

In summary, we have identified two main stages of the unrest (Fig. 5). The first stage (Phases I-II), with the migration of an energetic seismic swarm from deep to shallow depth, is consistent with the propagation of a magmatic dyke through the whole crust. The second stage (Phases III-IV), with simultaneous VLP and VT activity and large deflation, suggests the evacuation of a sub-Moho, large reservoir and a multifaceted interaction between magma and host rock.

The energetic seismic swarms in Phase I marks, to our knowledge, the first case of vertical propagation of a dyke traced for >25 km from a deep magma reservoir to the surface, although dykes have been observed to propagate horizontally for longer distances<sup>27-28</sup>. Dyke-induced swarms of this magnitude are rare and attributed to large intruded volumes, which scale with the moment of induced events as a power law<sup>29</sup>. According to this model, the cumulative moment of Phases I-II,  $M_0 = 2 \cdot 10^{18}$  Nm, would correspond to a dyke volume of  $5 \cdot 10^{-2}$  km<sup>3</sup>. Strike-slip focal mechanisms have been observed for other propagating dykes<sup>28, 30-33</sup>. Phase II involves a lateral dyke propagation, with VTs migrating 10-20 km towards South and reaching the seamount location<sup>20</sup>. The relative VT quiescence in Phase III is consistent with the establishment of an open pathway to the surface. High-rate crustal deformation sets on a week after the beginning of Phase III, consistent with the time needed for magma to widen its pathway by conduit erosion and establish a high flow rate<sup>34</sup>. Taken together, these observations suggest that the end of Phase II may mark the onset of the submarine eruption. During Phase IV, VTs, VLPs and ground deformation appear interlinked mechanically. VTs plausibly trigger VLPs and accompany the slow evacuation of the magma reservoir (Fig. 2d,f).

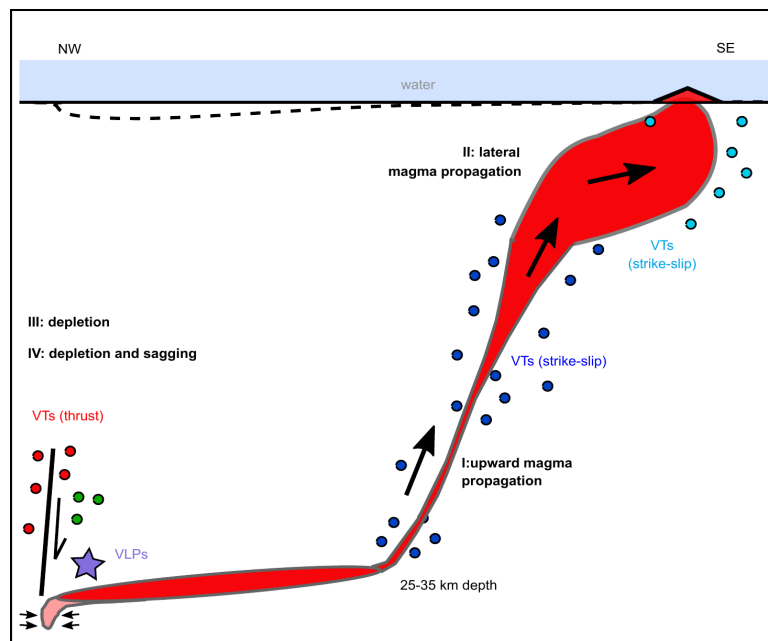


**Fig. 5 | Summary schematic.** A thin, subhorizontal reservoir feeds a dyke propagating first upward (Phase I) and later laterally southward (Phase II). The drainage of the reservoir's western edge triggers failure of the overlying rock, whose pressure pulses in turn trigger resonance in the reservoir (Phases III and IV).

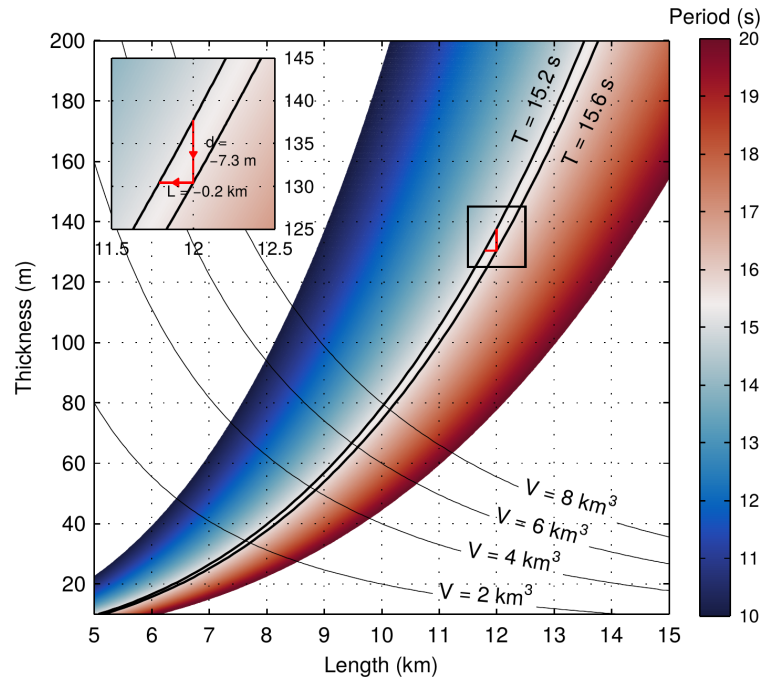


**Fig. 6 | Resonance period of a magma-filled crack as a function of crack length and thickness.**

Thick black lines are periods of 15.2 and 15.6 s that comprise the dominant periods of VLPs analysed here. Contours of reservoir volumes are shown as thin black lines. Zoomed inset shows an example geometry pathway involving first thinning at constant  $L$  and then shortening at constant  $d$  for the example length of 12 km.

VLPs may have different causes, but ringing events such as those observed at Mayotte have previously been explained by the resonance caused by slow standing waves trapped at the fluid-

solid interface of a fluid-filled crack or conduit<sup>2, 35-36</sup>. Here, their period and duration are especially long, which may be explained by the large size of the crack<sup>20</sup>, the stronger host rock because of the depth and basalt as the fluid filling the crack<sup>3</sup>. We use analytical formulas<sup>37</sup> to constrain crack geometry based on the dominant VLP period, which we assume is the fundamental resonance mode. Fundamental periods of 15.2-15.6 s are possible for a wide range of lengths and thicknesses (Fig. 6). However, cracks with  $L < 8$  km have too little volume to expel more than 1.5 km<sup>3</sup> of magma. A crack with  $L > 15$  km is unlikely, given the distribution of seismicity (Fig. 1). Smooth dominant period changes from 15.2 to 15.6 s and back may result first from the crack predominantly thinning and next shortening (Fig. 6). For example, path for  $L = 12$  km carries a volume loss of 1.6 km<sup>3</sup>. Thus, the change of dominant period may be entirely explained in terms of geometry changes consistent with the observed volume loss; variations in other parameters such as melt compressional wave velocity are also possible.

VLPs in combination with VTs have often been observed before and during caldera collapses<sup>18, 38-42</sup>. For example, VLPs occurred before and during the 2000 caldera collapse at Miyakejima, Japan, both with oscillating signals<sup>39</sup> and 20-50 s single pulse source time functions<sup>38, 40</sup>. With a maximum duration of ~60 s they were considerably shorter than those at Mayotte; their modelled source mechanism also had a different geometry<sup>38-40</sup>. They were interpreted as the resonance of an axially symmetric structure in response to a shallower trigger<sup>39</sup> or as resulting from the intermittent sinking of a vertical piston into the magmatic chamber, causing its sudden volumetric change<sup>38, 40</sup>. At Piton de la Fournaise, La Reunion island, 0.02-0.50 Hz VLPs have been attributed to repeated piston-like collapse<sup>42</sup>. The thrust mechanisms of typical VTs in Phase IV, inconsistent with the NE-SW transtensional background stress regime, require a strong stress perturbation, likely provided by the evacuation of the magma reservoir. Steep outward dipping faults are typically formed in the early stage of reservoir roof failure upon depletion<sup>43-44</sup>. They occur on newly formed, distributed faults (as



suggested by their small magnitude and existence of several families), rather than on a ring fault, confirming that the faulting is weakening the overlying material rather than representing the slip of a coherent block. As they are close above the reservoir, they may exert an efficient pressure pulse and trigger waves at the fluid-solid interface travelling towards the opposite edge of the reservoir and back, thereby producing a ringing signal<sup>3</sup>. The observed anti-correlated VT pairs (Fig. 4c) may be explained by the reverse motion on a fault, similar to observations during collapse events at calderas<sup>45</sup>. The January 2018 VLP, observed before the dyke had formed, suggests that the oscillator is a portion of the deep reservoir rather than the feeder dyke, and that the reservoir then had a similar size and shape.

Our deformation models locate a volume loss of at least  $1.3 \text{ km}^3$  at 25-35 km depth below the point where the four GNSS displacement vectors converge, which coincides spatially with the downsag seismicity and whose size is consistent with the variations of the VLP dominant period. A simple hypothesis is that the easternmost edge of the reservoir corresponds with the location of the earliest seismicity burst, later seen to migrate upwards. Thus, two questions remain: assuming a 15 km long reservoir, why is volume loss at the western edge and not the centre of the crack, and why is the shrinking horizontal rather than vertical? Reconciling the evidence suggest that a dipping sill-shaped reservoir loosing buoyant magma would shrink at its deeper portion, here to the West, and one-sided drainage coupled mechanically with the reservoir's failing roof may explain the observed horizontal shrinking pattern. Alternatively, a more complex sill shape, with a vertical westernmost portion, could account for the crustal deformation pattern. Superposition of outward dipping thrust faulting are equivalent to a vertical positive CLVD<sup>46</sup>, which may explain the model derived from the geodetic data.

In conclusion, our analysis suggests that a subhorizontal magma reservoir of up to 15 km in length lies between the newly discovered seamount<sup>20</sup> and Mayotte. Its exceptional depth of  $30 \pm 5$  km makes it the deepest reservoir whose evacuation has been observed in ground displacement data. Preliminary estimates suggest that more than  $3.4 \text{ km}^3$  of magma effused at the seafloor<sup>20</sup>, making it also the largest geophysically monitored submarine eruption to date. The mechanical processes activated offshore Mayotte represent a scaled-up version of a caldera formation process at its nucleating, downsag stage<sup>43</sup>. Phase IV, currently in progress, involves the growth of deep faults at the western edge of the emptying reservoir. Observations and modeling of reservoir depletion<sup>43</sup> suggest that, should it continue, fault growth will affect a progressively wider area and become shallower. A particular hazard is posed by a scenario where the outward dipping faults reach the ocean floor causing the entire block to collapse abruptly, and new normal faults begin to propagate upward, reaching closer to Mayotte. We estimate the volume evacuation threshold needed to trigger such a collapse,  $V_{\min}$ , based on an equation developed for calderas<sup>47</sup>:

$$V_{\min} = \frac{10 f \rho g h^2 r^2}{\kappa} \quad (1)$$

where  $f$  is rock friction coefficient,  $\rho$  is average medium density,  $g$  is gravitational acceleration,  $h$  is reservoir depth,  $\kappa$  is magma bulk modulus,  $r$  is reservoir radius. Using  $f = 0.6$ ,  $\rho = 2700 \text{ Kg m}^{-3}$ ,  $h = 25 \text{ km}$ ,  $r = 7.5 \text{ km}$ ,  $\kappa = 25 \text{ GPa}$  we obtain a threshold volume of  $230 \text{ km}^3$ , which is  $\sim 50$  times the volume of the seamount on May 2019. This scenario appears remote at this stage, but critical to monitor any migration of seismicity or change of focal mechanisms, as well as better constrain reservoir and faults geometry and crustal properties.

## Data availability

Seismic data used in this study pertain to networks II<sup>48</sup>, IU<sup>49</sup>, GE<sup>50</sup>, G<sup>51</sup>, PF<sup>52</sup> and RA<sup>53</sup> and are available at IRIS (Incorporated Research Institutions for Seismology), GEOFON (GEO-ForschungsNetz), ORFEUS EIDA (Observatories and Research Facilities for European Seismology - European Integrated Data Archive) and/or the Réseau Sismologique et Géodésique Français (French seismological and geodetic network, RESIF<sup>53</sup>) web services. Geodetic data are available at the web facilities of the Nevada Geodetic Laboratory, at the University of Nevada, Reno<sup>54</sup>.

### **Code availability**

All codes used in this work are open source. The codes used to generate individual results are available through the contact information from the original publications. Requests for further materials should be directed to S.C. (simone.cesca@gfz-potsdam.de).

### **Additional information**

Supplementary information is available in the online version of the paper.

### **References**

1. Lemoine, A. et al. The volcano-tectonic crisis of 2018 east of Mayotte, Comoros Islands. EarthArXiv, DOI: 10.31223/osf.io/d46xj (2019).
2. Ohminato, T., et al. Waveform inversion of very-long-period impulsive signals associated with magmatic injection beneath Kilauea volcano, Hawaii. *J. Geophys. Res.* **103**, 839–862 (1998).
3. Kumagai, H. & Chouet, B. A. Acoustic properties of a crack containing magmatic or hydrothermal fluids. *J. Geophys. Res. Solid Earth* **105**, 25493–25512 (2000).
4. Scrutton, R. A. et al. Constraints on the motion of Madagascar with respect to Africa. *Mar. Geol.* **43**, 1–20 (1981).

5. Phethean, J. et al. Madagascar's escape from africa: A high-resolution plate reconstruction for the Western Somali basin and implications for supercontinent dispersal. *Geochem. Geophys. Geosyst.* **17**, 5036–5055 (2016).
6. Reeves, C. The position of Madagascar within Gondwana and its movements during Gondwana dispersal. *J. Afr. Earth Sci.* **94**, 45–57 (2014).
7. Geiger, M. et al. Reappraisal of the timing of the breakup of Gondwana based on sedimentological and seismic evidence from the Morondava basin, Madagascar. *J. Afr. Earth Sci.* **38**, 363–381 (2004).
8. Coffin, M. & Rabinowitz, P. D. Reconstruction of Madagascar and Africa: Evidence from the davie fracture zone and western Somali basin. *J. Geophys. Res.* **92**, 9385–9406 (1987).
9. Jokat, W. et al. Timing and geometry of early Gondwana breakup. *J. Geophys. Res.* **108**, B9 (2003).
10. Leinweber, V. T. & Jokat, W. The Jurassic history of the Africa - Antarctica corridor - new constraints from magnetic data on the conjugate continental margins. *Tectonophysics* **530**, 87–101 (2012).
11. Mahanjane, E. S. A geotectonic history of the Northern Mozambique basin including the Beira high – a contribution for the understanding of its development. *Mar. Petrol. Geol.* **36**, 1–12 (2012).
12. Mahanjane, E. S. The Davie ridge and adjacent basins in the offshore Mozambique margin – a new insights for the hydrocarbon potential. *Mar. Petrol. Geol.* **57**, 561–571 (2014).
13. Emerick, C. & Duncan, R. Age progressive volcanism in the Comores Archipelago, western Indian Ocean and implications for Somali plate tectonics. *Earth Planet. Sci. Lett.* **60**, 415–428 (1982).
14. Nougier, J. et al. The Comoros Archipelago in the western Indian Ocean: volcanology geochronology and geodynamic setting. *J. Afr. Earth Sci.* **5**, 135–145 (1986).

15. Michon, L. The volcanism of the Comoros archipelago integrated at a regional scale. In *Active Volcanoes of the Southwest Indian Ocean* (eds Bachelery, P., Lénat, J.-F., Di Muro, A. & Michon, L.) 233–244 (Springer-Verlag, 2016).
16. Audru, J. et al. Major natural hazards in a tropical volcanic island: a review for Mayotte island, Comoros archipelago, Indian Ocean. *Eng. Geol.* **114**, 364–381 (2010).
17. Delvaux, D., & Barth, A. African stress pattern from formal inversion of focal mechanism data, *Tectonophysics*, **482**, 105–128 (2010).
18. Stamps, D. S., et al. Geodetic strain rate model for the East African rift system, *Scientific Reports*, **8**(1), 732, (2018).
19. Cesca, S., et al. Seismic catalogues of the 2018-2019 volcano-seismic crisis offshore Mayotte, Comoro Islands, GFZ Data Services, <http://doi.org/10.5880/GFZ.2.1.2019.004> (2019)
20. French Ministry of Research and French Ministry of Ecological and Solidarity Transition, Press Release, 16/05/2019 (2019).
21. Kumagai, H. et al. Magmatic dike resonances inferred from Very-Long-Period seismic signals. *Science* **299**, 2058–2061, (2003).
22. Aster, R. et al. Very long period oscillations of Mount Erebus volcano. *J. Geophys. Res. Solid Earth* **108**, B11 (2003).
23. Talandier, J. et al. Unusual seismic activity in 2011 and 2013 at the submarine volcano Rocard, Society hot spot (French Polynesia). *Geophys. Res. Lett.* **43**, 4247–4254 (2016).
24. Nikkhoo, M. et al. Compound dislocation models (CDMs) for volcano deformation analyses. *Geophys. J. Int.*, ggw427 (2017).
25. Heimann, S. et al. Grond - a probabilistic earthquake source inversion framework. V. 1.0. GFZ Data Services, <http://pyrocko.org/grond/docs/current/> (2018).

26. Davis, P. M., Surface deformation due to inflation of an arbitrarily oriented triaxial ellipsoidal cavity in an elastic half-space, with reference to Kilauea volcano, Hawaii, *J. Geophys. Res.: Solid Earth*, **91**, 7429–7438 (1986).
27. Uhira, K., & Toriyama, N. Meeting with the May 29, 2015 eruption of Kuchinoerabujima volcano. *Bull. Volcanol. Soc. Jpn.* **60**, 487-490 (2015).
28. Sigmundsson, F. et al. Segmented lateral dyke growth in a rifting event at Bárðarbunga volcanic system, Iceland. *Nature* **517**, 191–195 (2015).
29. White, R. & McCausland, W. Volcano-tectonic earthquakes: A new tool for estimating intrusive volumes and forecasting eruptions. *J. Volcanol. Geotherm. Res.* **309**, 139–155 (2016).
30. Hayashi, Y. & Morita, Y. An image of a magma intrusion process inferred from precise hypocentral migrations of the earthquake swarm east of the Izu peninsula. *Geophys. J. Int.* **153**, 159–174 (2003).
31. Passarelli, L. et al. Stress changes, focal mechanisms, and earthquake scaling laws for the 2000 dike at Miyakejima (Japan). *J. Geophys. Res. Solid Earth* **120**, 4130–4145 (2015).
32. Ruch, J., et al. Oblique rift opening revealed by reoccurring magma injection in central Iceland. *Nature communications* **7**, 12352 (2016).
33. Ágústsdóttir, T. et al. Strike slip faulting during the 2014 Bárðarbunga Holuhraun dike intrusion, central Iceland. *Geophys. Res. Lett.* **43**, 4, 1495-1503 (2016).
34. Wadge, G. The variation of magma discharge during basaltic eruptions. *J. Volcanol. Geotherm. Res.* **11**, 139–168 (1981).
35. Ferrazzini, V. & Aki, K. Slow waves trapped in a fluid-filled infinite crack: Implication for volcanic tremor. *J. Geophys. Res.* **92**, 9215–9223 (1987).
36. Chouet, B. Long-period volcano seismicity: its source and use in eruption forecasting. *Nature* **380**, 6572 (1996).

37. Maeda, Y. & Kumagai, H. A generalized equation for the resonance frequencies of a fluid-filled crack. *Geophys. J. Int.* **209**, 192–201 (2017).
38. Kumagai, H., et al. Very-Long Period Seismic Signals and Caldera Formation at Miyake Island, Japan. *Science*, **293** (5530), 687-690 (2001).
39. Kobayashi, T. et al. Very Long Period seismic signals observed before the caldera formation with the 2000 Miyakejima volcanic activity, Japan. *J. Geophys. Res. Solid Earth* **114**, B2 (2009).
40. Kobayashi, T. et al., Intermittent inflations recorded by broadband seismometers prior to the caldera formation at Miyake-jima volcano in 2000. *Earth Planet. Sci. Lett.*, **357-358**, 145-151 (2012).
41. Munekane, H. et al. Mechanisms of step-like tilt changes and very long period seismic signals during the 2000 Miyakejima eruption: Insights from kinematic GPS. *J. Geophys. Res. Solid Earth* **121**, 2932–2946 (2016).
42. Fontaine, F. R., et al. Very- and ultra-long-period seismic signals prior to and during caldera formation on La Reunion Island, *Scientific Reports*, **9**, 8068 (2019)
43. Acocella, V. Understanding caldera structure and development: An overview of analogue models compared to natural calderas. *Earth-Science Rev.* **85**, 125–160 (2007).
44. Levy, S. et al. Mechanics of fault reactivation before, during, and after the 2015 eruption of Axial seamount. *Geology* **46**, 447–450 (2018).
45. Jónsdóttir, K. et al. Evaluating changes of the Bárdarbunga caldera using repeating earthquakes. *AGU Fall Meeting Abstracts* (2017).
46. Cesca, S., & Heimann, S. Challenges in regional moment tensor resolution and interpretation. In *Moment Tensor Solutions: A Useful Tool for Seismotectonics* (ed D'Amico, S.), 163-181, (Springer, 2018).
47. Geshi, N. et al. Evaluating volumes for magma chambers and magma withdrawn for caldera collapse. *Earth Planet. Sci. Lett.* **396**, 107–115 (2014).

48. Scripps Institution of Oceanography. IRIS/IDA Seismic Network. International Federation of Digital Seismograph Networks. Dataset/Seismic Network. <https://doi.org/10.7914/SN/I> (1986)
49. Albuquerque Seismological Laboratory (ASL)/USGS. Global Seismograph Network (GSN - IRIS/USGS). International Federation of Digital Seismograph Networks. Dataset/Seismic Network. <https://doi.org/10.7914/SN/IU> (1988)
50. GEOFON Data Centre. GEOFON Seismic Network. Deutsches GeoForschungsZentrum GFZ. <https://doi.org/10.14470/tr560404>. (1993)
51. Institut De Physique Du Globe De Paris (IPGP), & Ecole Et Observatoire Des Sciences De La Terre De Strasbourg (EOST). GEOSCOPE, French Global Network of broad band seismic stations. Institut de Physique du Globe de Paris (IPGP). <https://doi.org/10.18715/geoscope.g> (1982)
52. PF: Piton de la Fournaise Volcano Observatory Network (Reunion Island), <https://www.fdsn.org/networks/detail/PF/> (last accessed 01 Aug 2019)
53. RESIF. RESIF-RAP French Accelerometric Network; RESIF - Réseau Sismologique et géodésique Français. DOI: <https://doi.org/10.15778/RESIF.RA> (1995).
54. Blewitt, G. et al. Harnessing the GPS data explosion for interdisciplinary science. *Eos* **99**, 4872–4886, <https://doi.org/10.1029/2018EO104623>, url: <http://geodesy.unr.edu> (last accessed 01 Aug 2019) (2018).

### **Corresponding author**

Correspondence and requests for materials should be addressed to Dr. Simone Cesca,

[simone.cesca@gfz-potsdam.de](mailto:simone.cesca@gfz-potsdam.de)

### **Acknowledgements**

The discovery of the underwater volcano is a result of the MAYOBS 1 campaign that took place from 2 to 19 May, 2019 aboard the Marion Dufresne oceanographic vessel. This campaign was



conducted by several French research institutions and laboratories (IPGP/CNRS/BRGM/IFREMER/IPGS) as part of a CNRS-INSU programme<sup>20</sup>. We thank CNRS-INSU for making public the location and size of the discovered volcano. M.I. thanks Dr. H. Sudhaus for her valuable contribution and acknowledges funding by the German Research Foundation DFG through an Emmy-Noether Young-Researcher-Grant (276464525). G.P. is funded by the German Research Foundation DFG project (362440331), a subproject of “SPP 2017: Mountain Building Processes in 4D” (Project Number 313806092). We thank Dr. Tim James and Mr. Timothy Davis for revising the English text.

### **Author contributions statement**

S.C. coordinated this project, conceived the manuscript and figures, and analysed, modeled and interpreted local accelerometric data. J.L. performed the VLP and array analysis. S.H. and H.R. performed the MT inversion for VT and VLP events. M.I., M.N. and L.P. analysed and modelled deformation data. G.P. assessed the seismic data quality. E.R., F.C. and T.D. contributed to the interpretation of results and discussion section. S.C., E.R., F.C. and T.D. drafted the manuscript. All authors reviewed the manuscript.

### **Finantial and non-financial competing interests**

The authors declare no competing interests.

### **Figure captions**

**Fig. 1 | Map view and cross sections of seismic and deformation sources.** **a**, Weak VT locations (points) and strong VT MTs (focal sphere, lower emisphere projections of the double-couple components in map view and backprojection of full MTs from East or South in the cross sections, respectively) plotted colour-coded according to similarity of waveform and distance to station

YTMZ (yellow triangle), overlay of 22 VLPs MTs (black focal spheres, negative CLVD convention used), best-fit point deformation sources (black symbols, SI), vertical displacements (black lines) and time evolution of horizontal displacements at four GNSS stations (black scatter points, 1 July, 2018 to 1 April, 2019), uncertainties within  $2\sigma$  of vertical displacements (green boxes, horizontal uncertainties negligible with respect to vertical ones), best fitting modelled displacements (red lines and arrows) and the inferred VLP source location (dashed red ellipses). The south-east and upward migration paths of seismicity and magma in Phases I-II (dashed black arrows in the cross-sections) reach the location of the discovered seamount<sup>20</sup> (orange circle and bars, assuming a 5 km diameter<sup>20</sup>). **b**, Map of the Comoro Islands, major regional tectonic structures and basin configuration<sup>5</sup>, showing fracture zones (thin lines) and earthquake locations and MTs prior to the sequence (circle and focal spheres, source GlobalCMT, GEOFON and USGS catalogues); shaded-relief topography and bathymetry from the ETOPO1 Global Relief Model from NOAA's National Centers for Environmental Information. The location of the study region is highlighted by a red star on the Earth globe.

**Fig. 2 | Timeline of the seismic sequence.** **a**, VT magnitudes (colour-coding as in Fig. 1) and seismicity rate (black line); **b**, VT depth based on MT inversion (circles) and array analysis (crosses); **c**, Differential S-P time of VTs at station YTMZ as a proxy of the distance to Mayotte (see SI for uncertainties); **d**, VLP magnitudes ( $M_s$ , purple circles) and rate (black line); **e**, VLP dominant periods (purple circles); **f**, Demeaned and detrended East, North, and vertical GNSS displacements at station MAYG; **g**, Normalized cumulative number of dyke-related VTs (blue line refers to blue, cyan and purple VTs in panels a-c), sagging-related VTs (red line refers to red and green VTs in panels a-c), VLPs (indigo line) and length of GNSS displacement vectors at station MAYG (green line). Sequence phases are marked in all panels with cyan vertical bars.

**Fig. 3 | MT solution for the 31 July, 2018 VLP.** **a**, The MT plot overlays the focal spheres of the ensemble of bootstrap solutions (SI). The red line denotes the overall best solution. The negative CLVD convention is applied. **b**, The resolved, oscillating source time function, with a dominant period  $T_R = 15.4$  s. **c**, Comparison of observed (red lines) and synthetic displacement traces (black lines), as well as their differences (red areas) for a selection of stations and components. Synthetic traces were computed assuming a continental (model P2017, see SI) or oceanic crust, based on station locations (Station name, spatial component, epicentral distance, azimuth, time window starting time, respect to the origin time, and time window duration are reported for each subplot).

**Fig. 4 | Example of seismic signals and spectra recorded at the YTMZ station.** **a**, 11 November, 2018 VLP. Waveforms correspond to normalized vertical acceleration filtered in different frequency bands; **b**, Stack of normalized vertical spectra for 51 VLPs (indigo bars represent integer multiples of the dominant frequency (0.065 Hz, or 15.4 s) with a red bar for the 2.5 multiple) **c**, anti-correlated waveforms for two VTs occurring 1.5 min apart on 20 August 2018 (time windows starting at 21:34:15.5 and 21:35:39.6 respectively). Waveforms of the first event (indigo) are compared to flipped waveforms of the second event (blue).

**Fig. 5 | Summary schematic.** A thin, subhorizontal reservoir feeds a dyke propagating first upward (Phase I) and later laterally southward (Phase II). The drainage of the reservoir's western edge triggers failure of the overlying rock, whose pressure pulses in turn trigger resonance in the reservoir (Phases III and IV).

**Fig. 6 | Resonance period of a magma-filled crack as a function of crack length and thickness.** Thick black lines are periods of 15.2 and 15.6 s that comprise the dominant periods of VLPs analysed here. Contours of reservoir volumes are shown as thin black lines. Zoomed inset shows an

example geometry pathway involving first thinning at constant  $L$  and then shortening at constant  $d$  for the example length of 12 km.

## **Methods**

Details about the methods used in this paper are given in the SI.

# **Drainage of a deep magma reservoir near Mayotte inferred from seismicity and deformation**

Simone Cesca<sup>1,\*</sup>, Jean Letort<sup>2</sup>, Hoby N. T. Razafindrakoto<sup>1</sup>, Sebastian Heimann<sup>1</sup>, Eleonora Rivalta<sup>1</sup>,  
Marius P. Isken<sup>3</sup>, Mehdi Nikkhoo<sup>1</sup>, Luigi Passarelli<sup>4</sup>, Gesa M. Petersen<sup>1,5</sup>, Fabrice Cotton<sup>1,5</sup> &  
Torsten Dahm<sup>1,5</sup>

<sup>1</sup> GFZ German Research Centre for Geosciences, Potsdam, Germany

<sup>2</sup> IRAP - Observatoire Midi Pyrénées, Toulouse, France

<sup>3</sup> University of Kiel, Germany

<sup>4</sup> King Abdullah University of Science and Technology (KAUST), Thuwal, Saudi Arabia

\* corresponding author [simone.cesca@gfz-potsdam.de](mailto:simone.cesca@gfz-potsdam.de)

## Supplementary Information

Supplementary Text, Supplementary Figures S1-S21, Supplementary Tables S1-S6.

### 1 Data

#### 1.1 Seismic data

Our five event catalogues<sup>1</sup>, namely: the weak VT events (detections and single station analysis), the strong VT events and the VLP events (detections and subset with MT inversion) catalogues, and the additional analyses on the relative depths of the VTs and moment tensor (MT) of the VLPs, were obtained using the following datasets (see also Fig. S1):

- Seismic stations at regional (up to 2500 km) epicentral distances were used to: a) detect VLP events, track the temporal variations of their spectral properties, and to invert for their MT; and b) locate centroids of strong VTs and invert for their MT. We used broadband data from the seismic networks II<sup>2</sup>, IU<sup>3</sup>, GE<sup>4</sup>, G<sup>5</sup>, and PF (Piton de la Fournaise Volcano Observatory Network, Reunion Island, OVPF).
- Station YTMZ of the Réseau Accélérométrique Permanent (French Accelerometrique Network, RA), as the only seismic station less than 100 km distance from the unrest region that operated continuously over the whole seismic sequence, was used to detect almost 7000 VT events, and to characterize a subset of 1904 VT events, by applying single station techniques.
- Teleseismic data from the Akbulak seismic array (ABKAR), Kazakhstan, was used for beamforming to detect the arrival time of direct P phase and seafloor converted pP and sP phases. The differential time between direct and seafloor reflected phases were used to infer the depth of VTs.

## 1.2 GNSS data

We used GNSS data from four stations on Mayotte island: GAMO (TERIA), KAWE (Lél@sarl), MAYG (CNES) and BDRL (TERIA) (Fig. S1). The data was processed and made available by the Nevada Geodetic Laboratory, at the University of Nevada, Reno<sup>6</sup>.

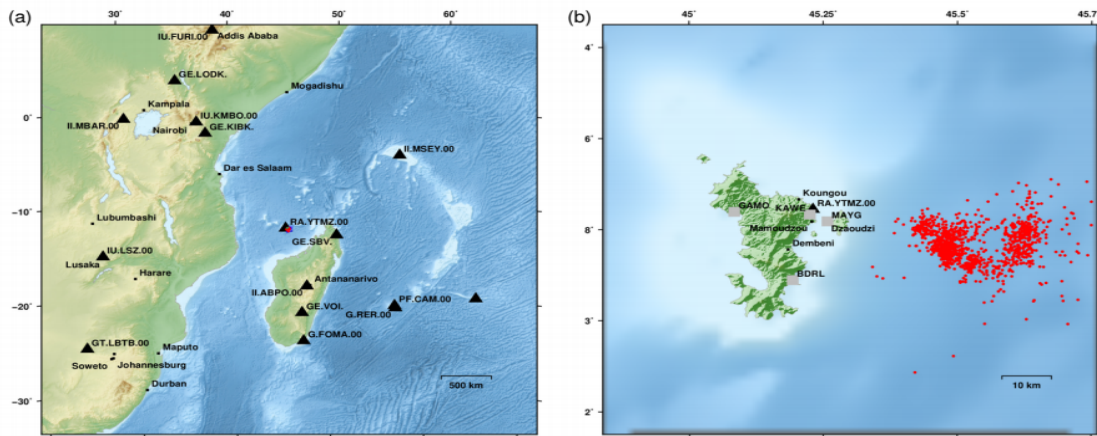


**Fig. S1 | Overview of the seismic and GNSS networks.** **a**, At regional distances, we relied on broadband seismic stations from II, IU, GE, G, PF and RA networks (black triangles); the target region is identified by a star. **b**, On Mayotte Island, seismicity and deformation signals were recorded by one strong motion sensor (YTMZ, black triangle) of the French Accelerometrique Network (RA) network and four GNSS sensors (grey squares). Single-station locations of VTs are marked in red.

## 1.3 Data quality assessment

In order to exclude systematic errors when inverting for the MT and in the polarization analysis, the data and metadata of all seismic stations were carefully evaluated using the AutoStatsQ toolbox<sup>7</sup>. Sensor orientations were verified using a Rayleigh wave polarization analysis<sup>7-9</sup>, considering a set of more than 25 teleseismic events with a homogeneous azimuthal distribution at each station. For each event and station the cross-correlation between the Hilbert-transformed R component and the

Z component in the time window containing Rayleigh waves are computed while rotating the horizontal components in 1 degree steps. A maximum cross-correlation obtained for zero rotation implies that the horizontal components of a sensor are correctly oriented. Amplitude gains of P phases were compared to synthetic data and among all stations to avoid problems arising from incorrect gain factors in the response functions or from unexpected site amplifications. Large timing errors on the order of several seconds were ruled out by assessing arrival times of teleseismic P phases across the network. Finally, power spectra computed from observed and synthetic data were compared as an additional check of gain levels and of reliable frequency ranges for MT inversion<sup>7</sup>. Synthetic traces and the power spectra were computed using the python based seismology environment Pyrocko<sup>10-11</sup>. One station with erroneous gain (GE.KMBO) and one station with inverse polarity (IU.FURI.00) were excluded from the study.

As for local seismic data, we used three component data from channels CN (until 12 September 2018) and HN (later on) of station YTMZ. We found that the East and Vertical components of channel HN were swapped for the considered time span. This problem was first identified using teleseismic data, by comparing observed ratios of P wave amplitudes on different components for large ( $M > 6.5$ ) intermediate and deep focus (depth  $> 100$  km) earthquakes at YTMZ and at neighbouring stations. We confirmed this problem by using local VTs and from extremely high cross-correlation among CNE and HNZ traces (as well as among CNZ and HNE traces) for VTs occurring just before and after 12 September 2018 (the date when the available data switches from CN to HN data).

## **2. Velocity models**

The nature of the crust beneath Mayotte is debated: it has been proposed that the archipelago lies, as they lie on oceanic lithosphere resulting from the opening of the Somali Basin at 140 Ma or at the



transition between oceanic and continental crust<sup>12</sup>. However, some of their lavas contain sandstone xenoliths dated at 533 Ma (pan African), pointing at the continental nature of the underlying crust<sup>13</sup>. Since the assumption of different crustal models and Moho depths can have a significant impact on some of the derived earthquake source parameters, such as their depth, magnitude and focal mechanism, we consider a range of crustal models, representing the current but limited knowledge on the crust structure in the region. For the seismological analysis<sup>14</sup> we consider 4 velocity models (Fig. S2 and Tables S1-S4). The first, which we will refer to as P2017, was recently proposed based on a tomography study<sup>15</sup> and includes a relatively thick crust of 33.5 km. The second model (CRUST1), was chosen from the CRUST1.0 dataset for the focal region<sup>16</sup>, removing the water layer. In this model, the crust is much thinner, with a thickness of only ~14.5 km. The third model (P2017B) is a modified version of the P2017 model, by thinning each layer to have a Moho depth of 22.3 km, a value in between the two previous models. Finally, a fourth model (CRUST2) has been used to reproduce regional data with an oceanic crust from the CRUST2.0 database<sup>17</sup>, used for all those stations where the source-station path is predominantly along oceanic crust. For the geodetic modelling, we consider 25 additional uniform realisations of a gradient model representing different crustal gradients and thicknesses between 15 and 30 km (black lines in Fig. S2).

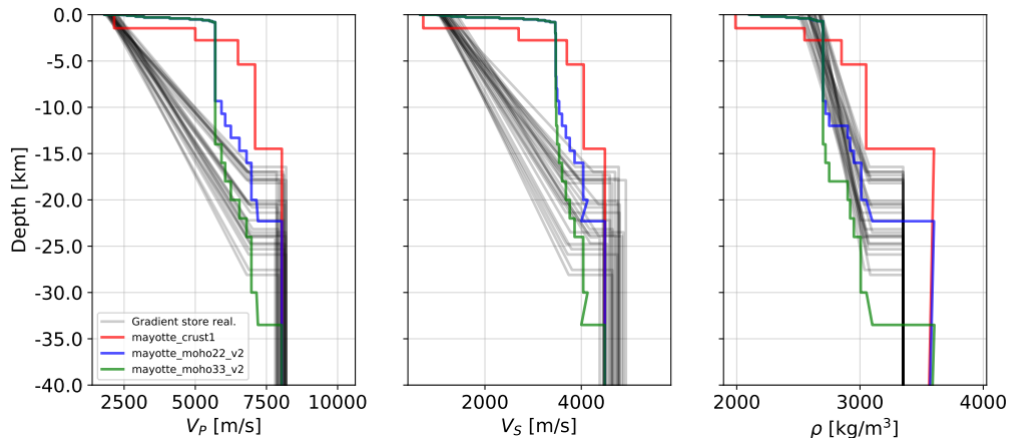


**Fig. S2 | Elastic earth models used for the Bayesian inversion with Grond<sup>14</sup>.** Models used for seismological applications are plotted with colour lines: green (P2017), blue (P2017B) and red (CRUST1). Additional crustal models for the geodetic modelling (black lines) are drawn from a uniform distribution. The surface  $V_p$  velocities range from 1.8 to 2.3 km/s, the deepest crustal  $V_p$  are distributed between 6.8 - 7.1 km/s.  $V_p/V_s$  ranges within  $\sqrt{3} \pm 10$ . The crustal densities ( $\rho$ ) vary between 2.5 - 2.7 g/cm<sup>3</sup> (surface) and 3.0 - 3.1 g/cm<sup>3</sup> (crustal base). The Moho depths are varied between 15 - 30 km with a fixed mantle density ( $\rho$ ) of 3.35 g/cm<sup>3</sup>.

**Tab. S1.** Parameters of the model P2017<sup>15</sup>.

Depth [km]	$v_p$ [km/s]	$v_s$ [km/s]	$\rho$ [Kg/m <sup>3</sup> ]
0.00-0.01	1.80	0.65	2.10
0.01-0.03	2.40	1.01	2.20
0.03-0.10	2.60	1.10	2.20
0.10-0.20	2.90	1.30	2.20
0.20-0.30	3.20	1.60	2.40
0.30-0.40	4.10	2.30	2.50
0.40-0.50	4.80	2.80	2.60
0.50-0.60	5.25	3.10	2.63
0.60-0.70	5.50	3.25	2.65
0.70-0.80	5.60	3.35	2.70
0.80-2.00	5.70	3.46	2.70
2.00-10.00	5.70	3.47	2.70
10.00-12.00	5.70	3.48	2.70
12.00-14.00	5.70	3.50	2.70
14.00-16.00	5.92	3.54	2.72
16.00-18.00	6.05	3.60	2.75
18.00-20.00	6.25	3.68	2.90
20.00-22.00	6.55	3.76	2.92
22.00-24.00	6.80	3.86	2.95
24.00-30.00	6.97	4.04	3.01
30.00-33.50	7.15	4.13	3.05
Moho			
33.50	8.04	4.49	3.60

**Tab. S2.** Parameters of the model CRUST1<sup>16</sup>.

Depth [km]	$v_p$ [km/s]	$v_s$ [km/s]	$\rho$ [Kg/m <sup>3</sup> ]
0.00-1.46	2.15	0.72	1.99
1.46-2.76	5.00	2.70	2.55
2.76-5.37	6.50	3.70	2.85
5.37-14.48	7.10	4.05	3.05
Moho			
14.48	8.14	4.52	3.35

**Tab. S3.** Parameters of the model P2017B, modified after P2017<sup>15</sup>, to have a 22.3 km thick crust.

Depth [km]	$v_p$ [km/s]	$v_s$ [km/s]	$\rho$ [Kg/m <sup>3</sup> ]
0.00-0.01	1.80	0.65	2.10
0.01-0.03	2.40	1.01	2.20
0.03-0.10	2.60	1.10	2.20
0.10-0.20	2.90	1.30	2.20
0.20-0.30	3.20	1.60	2.40
0.30-0.40	4.10	2.30	2.50
0.40-0.50	4.80	2.80	2.60
0.50-0.60	5.25	3.10	2.63
0.60-0.70	5.50	3.25	2.65
0.70-0.80	5.60	3.35	2.70
0.80-2.00	5.70	3.46	2.70
2.00-6.67	5.70	3.47	2.70
6.67-8.00	5.70	3.48	2.70
8.00-9.33	5.70	3.50	2.70
9.33-10.70	5.92	3.54	2.72
10.70-12.00	6.05	3.60	2.75
12.00-13.30	6.25	3.68	2.90
13.30-14.70	6.55	3.76	2.92
16.00-20.00	6.80	3.86	2.95
16.00-20.00	6.97	4.04	3.01
20.00-22.30	7.15	4.13	3.05
Moho			
22.30	8.04	4.49	3.60

**Tab. S4.** Parameters of the oceanic crustal model CRUST2<sup>17</sup>.

Depth [km]	$v_p$ [km/s]	$v_s$ [km/s]	$\rho$ [Kg/m <sup>3</sup> ]
0.00-2.00	5.00	2.50	2.60
2.00-4.00	6.60	3.65	2.90
4.00-7.00	7.10	3.90	3.05
Moho			
7.00	8.04	4.49	3.60

### 3. 3. Characterisation of large VTs using regional and teleseismic data

#### 3.1 VT centroid moment tensor inversion

We estimated centroid MTs for the largest VTs using a Bayesian bootstrap method (Grond<sup>14</sup>). This probabilistic optimization assesses the earthquake source parameters as non-parametric posterior distribution in the form of a solution ensemble. We used waveform data from local strong motion station (YTMZ) and regional stations (Fig. S1). The number of usable stations varies from one event to the other, depending on the signal-to-noise ratios. For the forward modelling, synthetic seismograms were computed using Green's functions for different velocity models, resembling continental and oceanic crusts. For local distances and continental crust ray paths, we tested different velocity models (Tables S1-S3). For oceanic crust ray paths, we select a representative profile from the CRUST 2.0 database<sup>17</sup> (Table S4).

In the MT inversion, full waveforms were fitted in time domain, in a frequency range of 0.01 - 0.03 Hz. We established a workflow involving three-steps: (1) Run the inversion for the largest event ( $M_w$  5.9); (2) Repeat the inversion, fixing the centroid location to the result of (1), but now allowing for time shifts between observed and synthetic seismograms; and (3) Run the inversion for all events, using the obtained time shifts from (2) as corrections to compensate mismodelling.

One example of a MT inversion result is shown in Fig. S3, using a combination of the PR2017 and CRUST2 models for the continental and oceanic crust. Given the uncertain velocity structure at Mayotte, we tested alternative continental crust models, with thinner crustal thickness (models PR2017B and CRUST1). Resulting MT solutions for the 67 large VTs dataset are illustrated in Fig. S4 where the full MT solutions show some minor variation for a few VT events and the double couple (DC) component is very stable. The temporal evolution of source parameters is shown in

Fig. S5; a smooth variation of the isotropic and CLVD component accompanies the upward migration of seismicity by the end of Phase I and continues in Phase II.

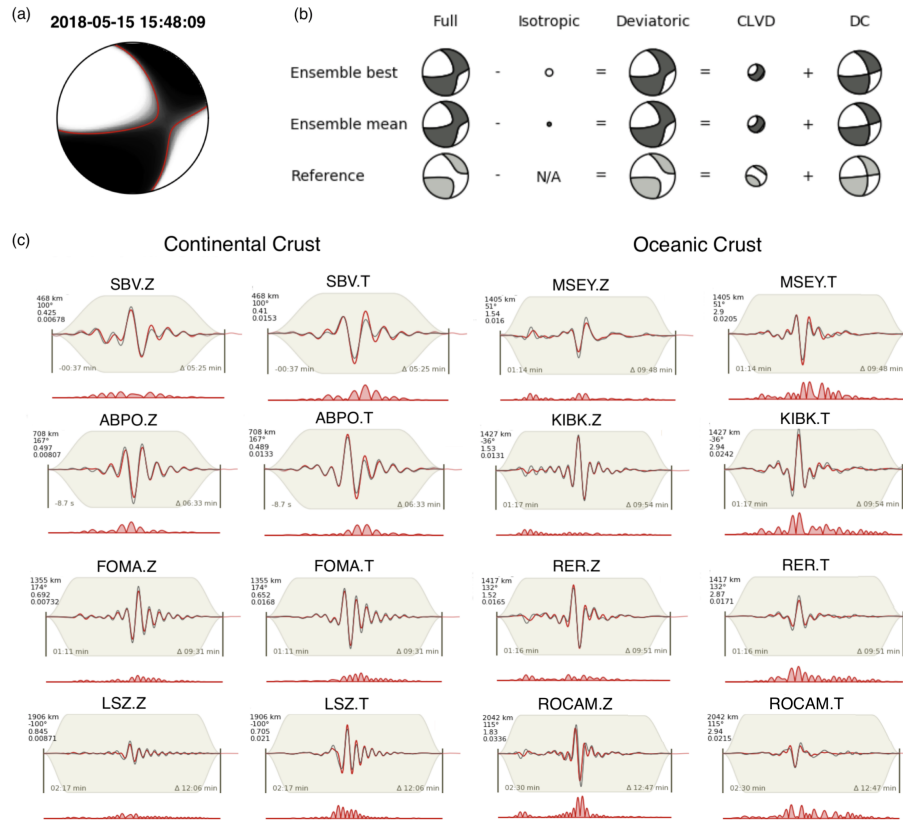


**Fig. S3 | Example of MT solution for the largest VT event on 15 May 2018  $M_w$  5.9 using velocity models PR2017 and CRUST2. **a**, Overlay of the focal spheres for the ensemble of best solutions. **b**, Standard MT decomposition for the best solution (the one minimizing misfit and using all stations), the mean solution (considering all good quality solutions and station bootstrapping<sup>14</sup>) and a reference solution (here the GEOFON solution). **c**, Comparison of observed (red lines) and synthetic displacement traces (black lines) as well as their differences (red areas) for a selection of stations and components.**

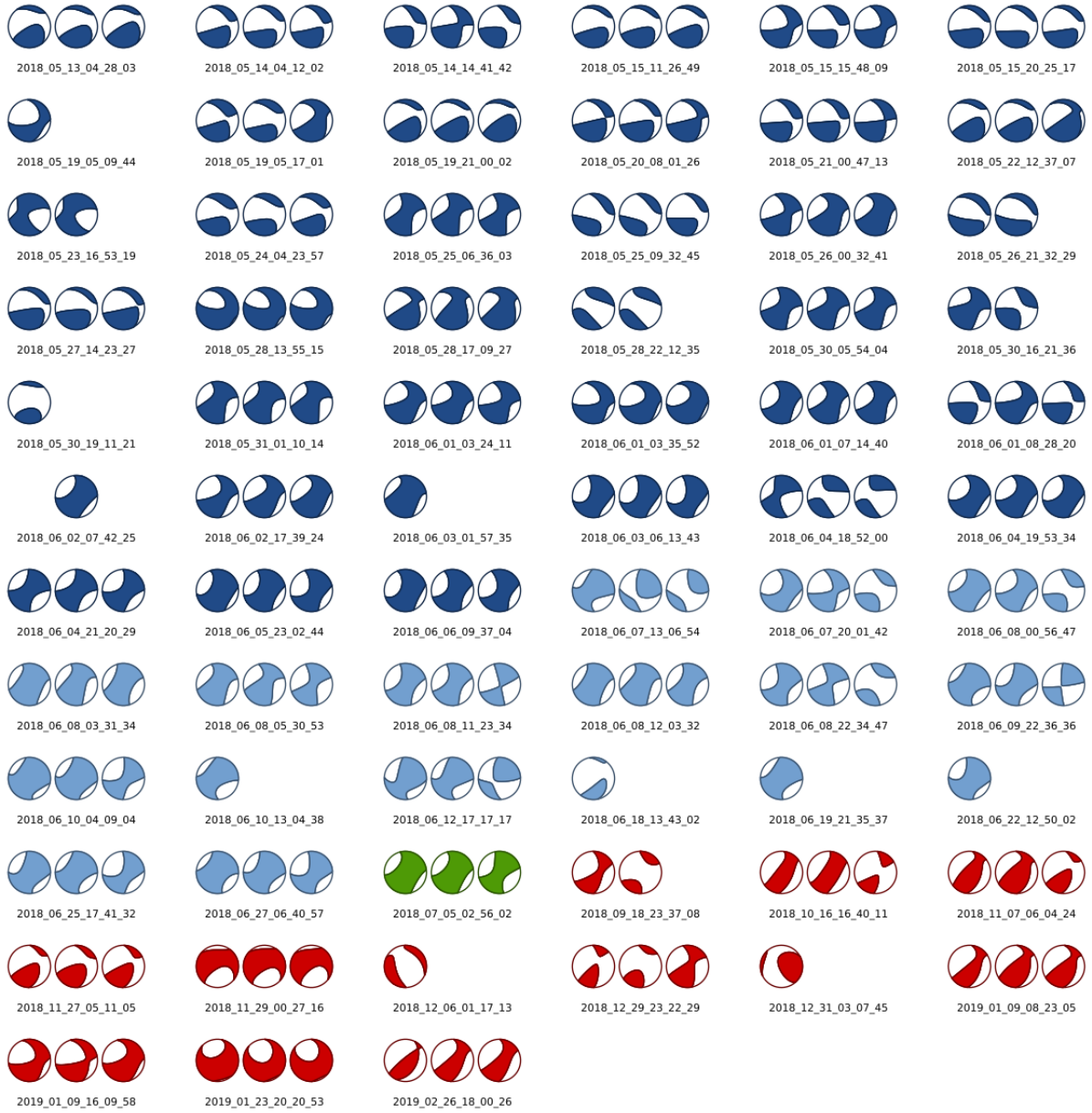


**Fig. S4 | Comparison of centroid MT solutions for the largest VT event on 15 May 2018  $M_w$  5.9, assuming a common oceanic model (CRUST2) and different continental models. a, P2017, crustal thickness 33.5 km. b, P2017B, crustal thickness 22.3 km, and c, CRUST1, crustal thickness 14.5 km. The scatter of the ensemble of acceptable centroid MT solutions (for details, see Grond<sup>14</sup>) is substantially reduced when assuming a crustal depth of 22 km.**

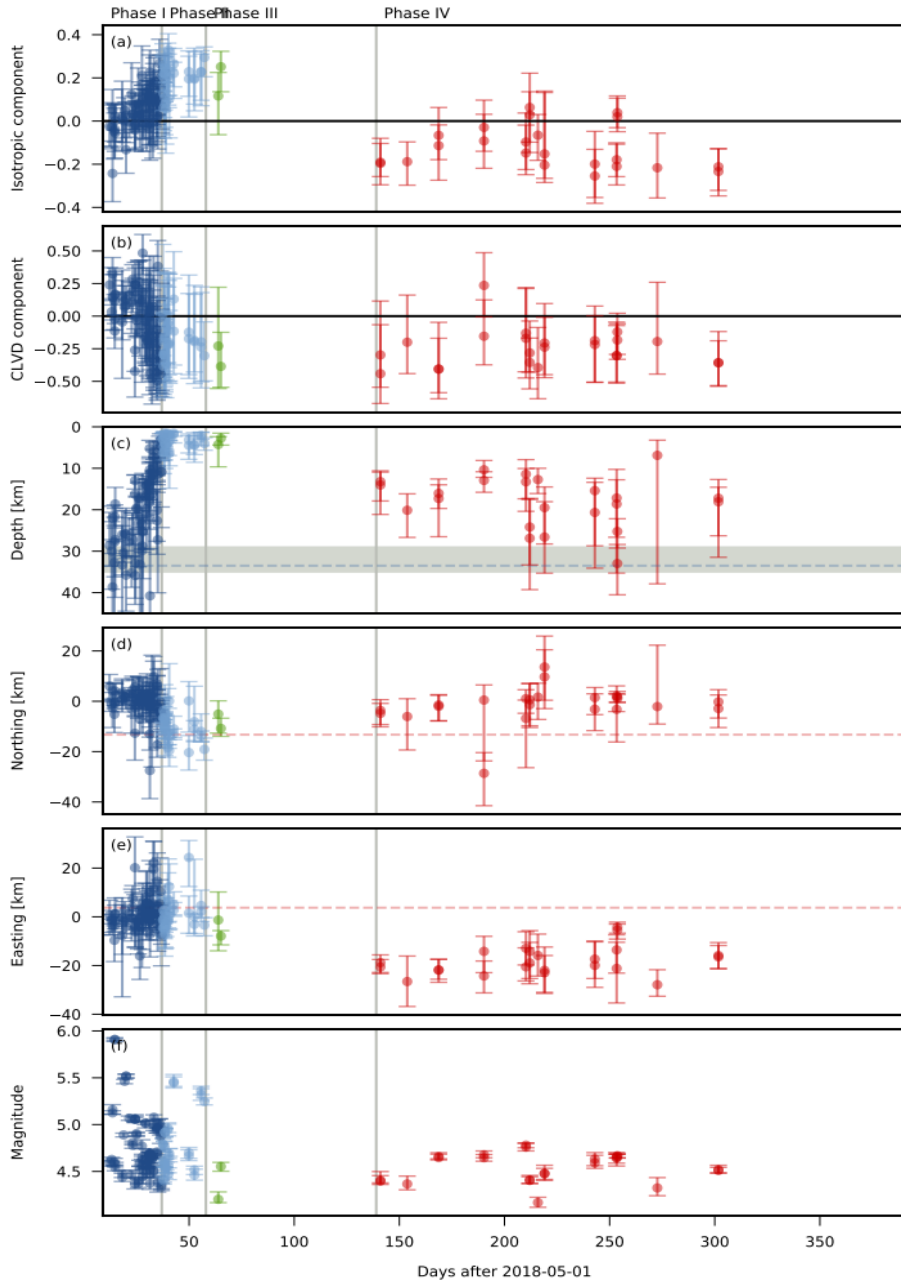


**Fig. S5 | Temporal evolution of VT source parameters and uncertainties as resolved by moment tensor inversion based on a bootstrap approach<sup>14</sup>.** Percentage of **a**, isotropic and **b**, CLVD components, **c**, centroid depth, **d**, northing and **e**, easting relative to reference location - 12.7977°N, 45.6805°E, and **f**, moment magnitude. The reservoir depth interval including uncertainties, is marked by a grey band in panel (c). The seamount location is marked in panels (d) and (e) as red dashed lines. This test was performed using velocity models P2017 and CRUST2.



### 3.2 Depth estimation

We took several precautions to ensure the quality of our depth estimations beyond our MT inversion results. Indeed, in poorly instrumented areas, estimating the depth of earthquakes is difficult.

Important epistemic uncertainties may arise from the assumed local/regional velocity models and the method used for depth estimation. Thus combining different methods and independent datasets is a good strategy to reduce such epistemic uncertainties<sup>18-20</sup>.

Here, we combined independent observations of teleseismic body-wave and regional surface-wave observations with information from different approaches. In particular, we complemented the MT inversion analysis, in which we inverted also for the centroid depth, with an analysis of teleseismic depth phases. This approach helped to tightly constrain the source depth based on the relative arrival times of waves traveling vertically upward and downward around the source. A correct estimate of the focal mechanism from regional data helped avoid misinterpretations of the detected depth phase (pP instead of sP). The overall good coherence among our results that was obtained using different datasets and approaches guarantees that our findings regarding the relative depth variations with time are robust.

#### 3.2.1 VTs depth estimation using local and regional data

Our estimates of centroid depths and their uncertainties for the 67 VTs in the *strongVT* regional catalogue, based on centroid MT inversion, showed that VTs migrated upward at the end of Phase I, between end of May and 7 June 2018 (Sec. 2.1 and Fig. S4). According to these estimates, seismicity migrates from ~30 km to less than 10 km depth, possibly eventually approaching the sea floor. This result confirms and extends previous findings<sup>21</sup>, based on local and regional data, that also identified a rough ascent of seismicity between ~35 - 40 km and ~10 - 15 km in the same time period.

The absolute depth estimates depended on the chosen crustal structure. In Fig. S6 we compare depth estimate for stage 1 and the beginning of stage 2. The centroid depths obtained assuming continental crusts of 15 to 33 km (models P2017, P2017B and CRUST1) resolve a clear upward migration by the end of May 2018, but the depth extent differs in the two cases. Interestingly, the deepest events always occur at the crust-mantle boundary.

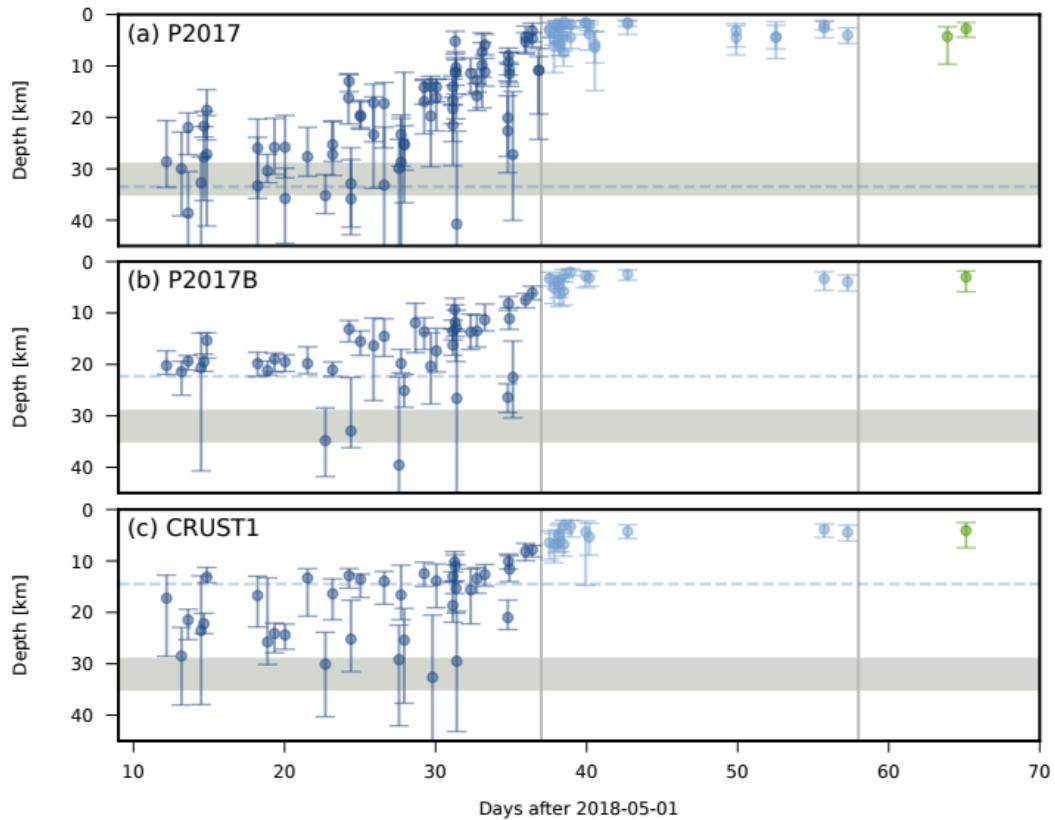


**Fig. S6 | Comparison of the temporal evolution of VT centroid depths with uncertainties as resolved by MT inversion using three velocity models.** The models have a crustal thickness of 33.5 km (**a**, model P2017), 22.3 km (**b**, P2017B) and 14.5 km (**c**, CRUST1) for the used continental model. The Moho depth is plotted for each model as cyan dashed line. The reservoir depth interval, considering uncertainties, is marked by a gray band in each plot.

### 3.2.2 VTs depth estimation using the ABKAR array data

We analysed teleseismic data from one CTBTO array that allowed for a reliable detection of the seismic sequence (ABKAR, Kazakhstan). The differential time between the direct P phase and seafloor reflected pP and sP phases was used to infer the hypocentral depth<sup>22</sup>. Teleseismic P-pP delays helped to obtain precise depth estimations<sup>23-26</sup>. Teleseismic depth phases are powerful tools for constraining relative depth variations, especially for depths between 10 - 80 km, where depth phases are usually visible and well-separated from the P-wave arrival. Comparing depth phases' arrivals from different earthquakes from the same area resulted in a robust and powerful methodology for relative depth estimations<sup>22, 27</sup>. A previous study<sup>22</sup> showed that by using one single teleseismic array, as we do in this study, it is possible to track precisely small depth variations below 5 km.

We used this approach to estimate the depth of the largest VTs and track the temporal variation of the average depth during the swarm, as follows. Assuming location and origin time from the reference catalogue for each Mw4+ event, and using the AK135 velocity model, we estimated the theoretical arrival time of the direct P wave at the ABKAR array. Continuous vertical component seismic data were downloaded for all chosen events and array stations, with a time window beginning 40 s before the theoretical P onsets and ending 100 s after. Raw data were then bandpass filtered between 0.8 and 2.5 Hz, and beamformed to have one single trace (beam) per event. The 0.8-2.5 Hz band was chosen here since teleseismic body wave arrivals were reliably detected in this frequency band and as a compromise between high mantle attenuation above 1 Hz and source radiation usually with higher energy above 0.5-1 Hz for moderate magnitudes events (M 4-5). We also tested higher and lower frequency bands, which resulted in a poorer resolution of pP phases. The direct P wave was manually picked for each trace; events without a clear P arrival were rejected. Beams were aligned according to the picked P-arrival time. For each event, superior and

inferior envelopes were computed, summed and the resulting trace was normalized by its norm. Finally, to better identify the temporal variation of reflected wave delays, a normalized average envelope was computed every 3 hours, using the envelopes of all events occurring in a 4-day time window, starting 2 days before  $T_i$  and ending 2 days after. Results are shown as function of time in Fig. S7.

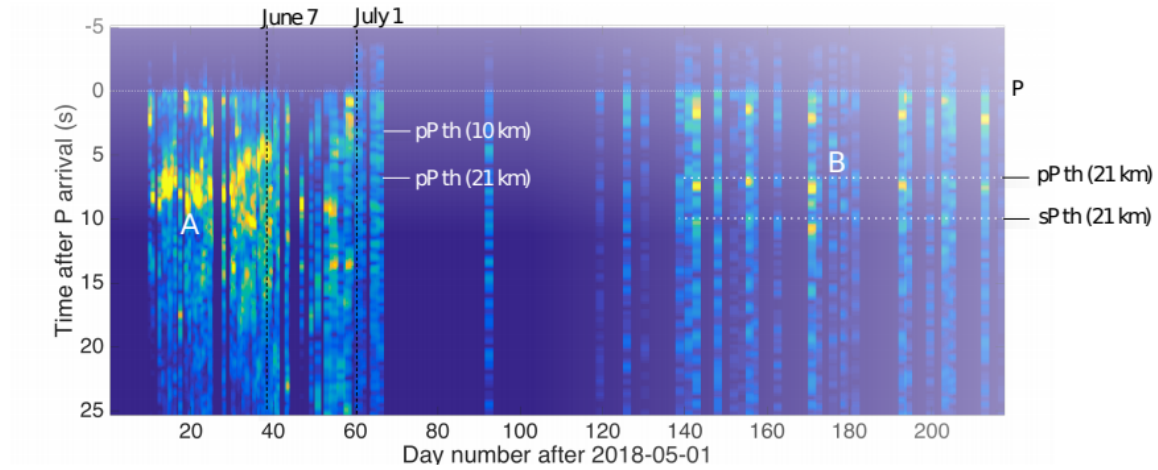


**Fig. S7 | Mean daily normalized beam envelopes at the ABKAR array, Kazakhstan.** The band identified by white dashed lines and marked with A denotes the arrival time of the identified depth phases, which have a delay of 8 - 10 s from the first P onset in early May (event 1) and only 4 - 5 s in early June, later increasing again to ~8 s.

The figure shows a clear, coherent and continuous variation of the delays of reflected waves inside the P-coda over time. They vary from 8 - 10 s in early May (event 1) to 4 - 5 s in early June (event 100). An absolute depth estimate was required to discriminate if the observed depth phases were pP/pwP or sP. pP/pwP were more likely to be detected, given the expected radiation pattern for the focal mechanism of the main events. The reflected waves were identified as pP and sP (pwP water multiples may be present as well). A decrease in reflected waves' arrival times was apparent at the end of May, supporting the upward migration of VT seismicity at the end of Phase I. Thus, the

upward migration of the largest VTs would be from about 25 to 10 km depth, and possibly reaching an even shallower depth by mid-June. Again, given the debated crustal structure at Mayotte, we tested three very different velocity models (P2017, P2017B, CRUST1), to check the stability of our results (Fig. S8). While the absolute depth values can be shifted (up to 8 km) depending on the chosen velocity model, the relative variations were similar for all tested models. These results support a clear upward migration at the end of Phase I, and a slightly shallower depth in Phase III-IV (sagging) with respect to the VTs in the early stage of Phase I (unrest at the reservoir).

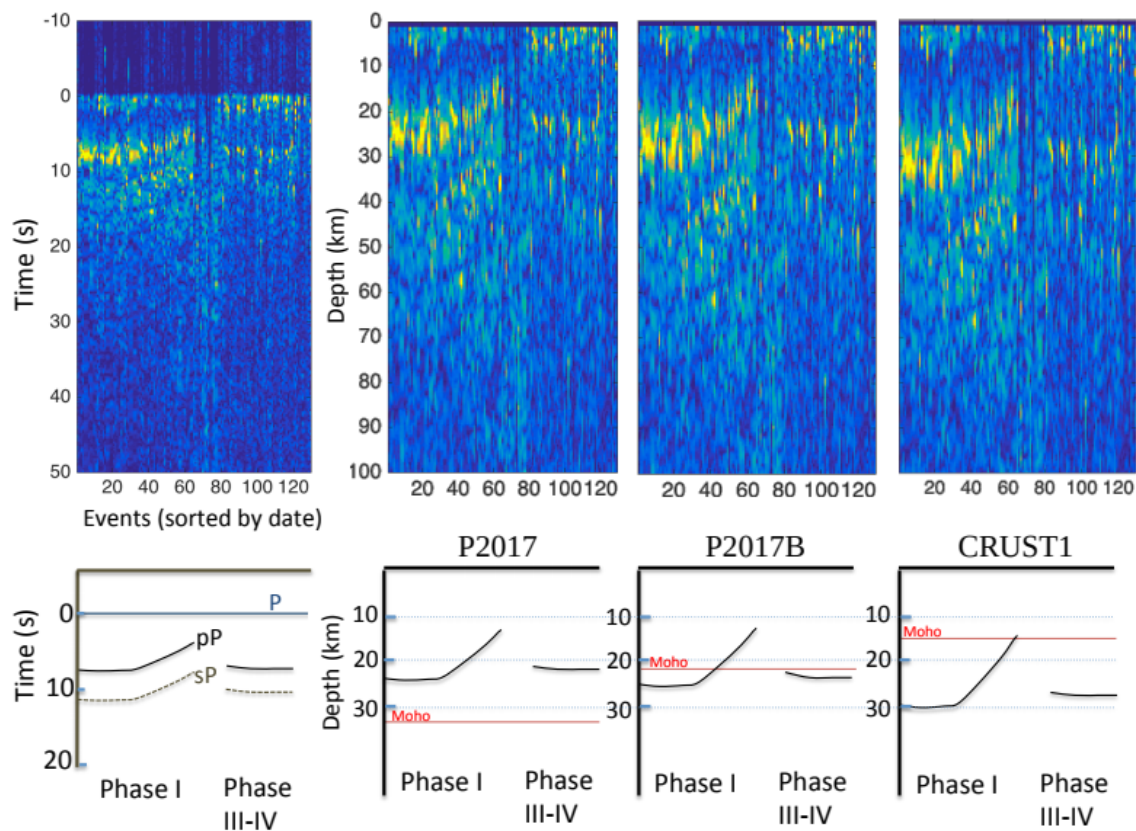


**Fig. S8 | Comparison of depth estimation using the ABKAR array, Kazakhstan, based on different velocity models: P2017, P2017B, CRUST1.** Observed time envelopes were converted into equivalent focal depths, assuming P-pP detections (top). These figures can be interpreted (bottom schemes) to show the average depth variations following the 3 models.

Beside the effect of the velocity model, a second source of uncertainty in the depth estimation concerns phase picking. Repeating the picking procedure for other frequency bands (1.5-3.0 Hz and 0.5-1.5 Hz) and consequently the depth estimation, we found an average difference of  $-0.5 \pm 1.1$  km and  $0.4 \pm 2.3$  km, respectively. Furthermore, we found 4 repeaters, identified with the regional stations ABPO and YTMZ, for which we had picked pP arrivals at the ABKAR array in Kazakhstan. For these events, the depth estimations are in the range  $23.1 \pm 1.7$  km, although the waveform similarity at regional distances suggest a similar depth for all them. The variability can be attributed to the pP picking procedure. In conclusion, both tests suggest that depth uncertainties due to the pP pickings can be estimated in about  $\pm 2$  km, thus much smaller compared to those due to the velocity model.

## **4 Weak VTs using single station analysis**

### **4.1 Catalogue generation**

Three-component continuous seismic records of the YTMZ station were visually scanned to identify the significant events listed by USGS and GEOFON, which jointly amount to 176 earthquakes above  $M_w$  4.0. YTMZ data had only a few gaps in September and November 2018. Thousands of events of the Mayotte sequence were included in the data. One day of continuous recordings with a high seismicity rate is shown in Figure S9. Signal detection and picking were performed manually, leading to the identification of 6990 events. We discuss here a subset of 1904 events with better signal quality, imposing a minimum moment magnitude of 3.5 and a minimum peak ground acceleration (after bandpass filtering between 0.2 and 4.0 Hz) of  $0.001 \text{ m/s}^2$ . The purpose of our single station analysis was not to provide an accurate location of weak VTs, but primarily to identify different families of VTs and investigate their time evolution using a large

dataset. A more accurate location of VTs was obtained for those with  $M > 4$  using the regional centroid centroid MT inversion.

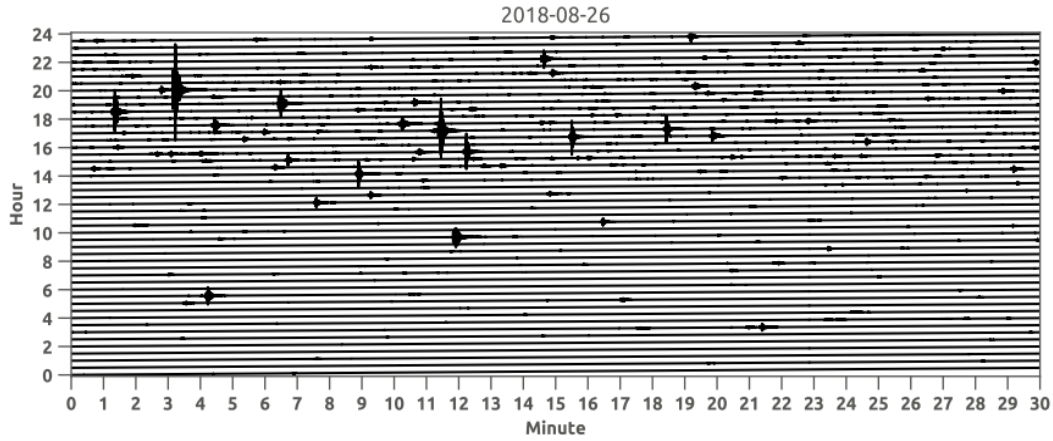


**Fig. S9 | Helicoidal plot for the 26 August 2018 at station YTMZ.** Raw vertical component waveforms, bandpass filtered between 0.2 and 5.0 Hz are shown.

#### 4.2 Waveform attributes

We computed the following VT waveform attributes: (1) differential S-P time as a proxy for the hypocentral distance to the focal region, (2) peak ground acceleration (PGA) as a proxy for magnitude, (3) P-wave particle motion rectilinearity and orientation, which provided information on the backazimuth, (4) the amplitude ratio among horizontal and vertical components of the P wave, which provided some qualitative information on the evolution of the incidence angle, and (5) the amplitude ratio for S and P waves, which provided information on the focal mechanism.

The differential S-P times, which were based on manual picking, were used to estimate the hypocentral distance along the ray path, assuming a mean crustal velocity of 6 km/s. The uncertainty of differential S-P time was small (we estimate below 0.1 s), since both P and S phases were manually picked and we considered only the cleanest VTs signals. S-P times were used to

infer a rough epicentral location assuming a fixed depth of 20 km (chosen as average centroid depth of large VTs as a result of the centroid MT inversion). A fixed depth was also assumed in previous studies at Mayotte to stabilize the location procedure with a poor local network<sup>21</sup>. Because of this bold assumption and despite the small uncertainty of the differential time, the epicentral distance uncertainties are large (more than 10 km).

To estimate magnitudes for the 1904 VT dataset, we proceeded as follows. Observed PGAs were first corrected for distance, assuming a common reference distance of 40 km (as an average value), and then plotted against moment magnitudes (for all events for which a magnitude from a MT solution was available). We then used the correlation between the logarithm of distance-corrected PGAs and  $M_w$  magnitudes, to establish a relation among these and to infer the moment magnitude of 1904 events based on the PGA at YTMZ and distance to this station.

The polarization analysis was performed using only the horizontal component of the P wave. For this purpose, we used raw acceleration data and applied a 4<sup>th</sup> order Butterworth filter between 0.2 and 4.0 Hz. We extracted 1.5 s time windows for P phases, starting at the time of the picked onset. The rectilinearity definition<sup>28</sup> depends on the ratio of the covariance matrix eigenvalues, and its derivation was implemented following the obspy library<sup>29</sup>. An example of particle motion and derived backazimuth is shown in Fig. S9 for the largest VT event of May 15, 2018. The average rectilinearity value for our 1904 events was 0.58, while the highest rectilinearity value was 0.86. We estimated a backazimuth uncertainty for the largest VT event (Figure S10a,b) of  $\sim 2^\circ$ ; this estimation was based on repeated analysis after random perturbation of the bandpass frequency corners in the range  $0.20 \pm 0.05$  Hz and  $4.0 \pm 1.0$  Hz and the time window length in the range  $1.50 \pm 0.15$  s. However, such uncertainty sums with the uncertainty on the sensor orientation. To verify the sensor orientation, we estimated the backazimuth for the largest VT event ( $104.5^\circ$ ) and compared it with



the theoretical value based on our own centroid location ( $96.1^\circ$ ), resulting in a sensor orientation correction of  $\sim 8^\circ$  anticlockwise. This static correction was applied to all backazimuth estimates (e.g. in the locations plotted in Fig. 2). Interestingly, a similar correction of  $\sim 7^\circ$  was also found when comparing the particle motion of the largest VLP to the theoretical backazimuth derived for the deformation source, located by fitting geodetic data (Fig. S10c,d).

Amplitude ratios (between S and P phase amplitudes, and between the vertical and horizontal components of the P phase) were measured from the maximal acceleration after bandpass filtering in the range 0.2 - 4.0 Hz and tapering 1.5 s time windows for P phases and slightly longer windows (2.5 - 4.0 s depending on the S-P times) for S phases, based on picked onsets. We used these values to judge the qualitative evolution of the VT seismicity with time. An overview of the estimated waveform attributes is shown in Fig. S11.

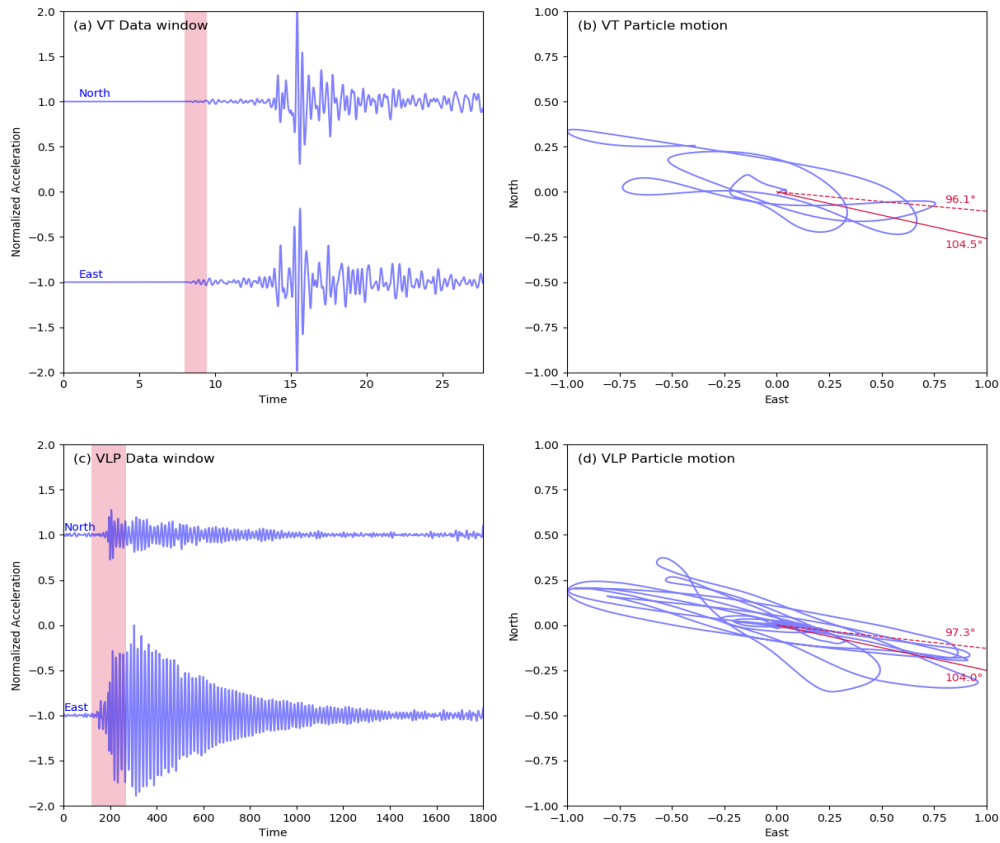


**Fig. S10 | Example of particle motion determination for the Mw 5.9 VT on 15 May 2018 (a, b) and the VLP signal of 11 November 2018 (c, d).** Horizontal components at station YTMZ (normalized accelerations) are shown for the VT (a) applying a bandpass filtered between 0.5 and 4.0 Hz, and VLP (c), with bandpass filter 0.063 – 0.08 Hz. The polarization analysis was performed on shorter time windows (red areas): 1.5 s long signal corresponding to the first P onset for the VT, and a time window of 150 s for the VLP. Hodograms for the horizontal particle motion can be used to estimate the backazimuth (red lines in **b, d** and compared with reference ones (dashed red lines in panels **b, d**). For the VT we predict a backazimuth of 104.5° as computed from the particle motion, which show a mismatch of  $\sim 8.4^\circ$  with respect to the backazimuth based on the regional MT inversion (96.1°). The VLP backazimuth estimated from the particle motion was compared to the backazimuth based on the location of the deformation source.

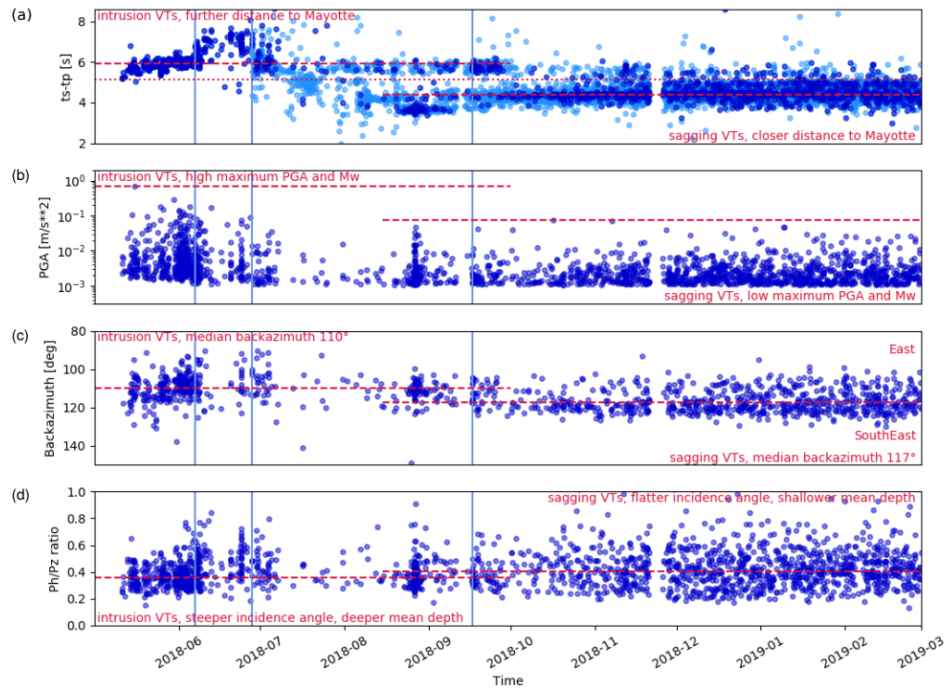


**Fig. S11 | Overview of the single station analysis using data from station YTMZ.** **a**, The temporal evolution of differential S-P times obtained upon picking 6990 VTs (light blue circles) denotes a dominance of larger hypocentral distances (differential time larger than 5.15 s), which dominate Phases I and II of the sequence, and correspond to intrusion-triggered VTs. In Phases III-IV, most VTs are associated with sagging processes at closer distances. For the largest 1904 events (dark blue), we could extract other attributes. **b**, Maximum PGAs were found for the intrusion related VTs, which also presented large magnitudes. **c**, The backazimuths varied between East and Southeast, with higher backazimuths for the sagging related events, whose epicenters were located closer to Mayotte than those of the intrusion-driven VTs. **d**, A broad range of Ph/Pz ratios at YTMZ indicated slightly steeper angles (deeper sources) for dike-related VTs than for sagging-related ones. The temporal evolution of this parameter supports the upward migration at the end of Phase 1 (Fig. 3). Dashed lines denote median values (maximal values for PGAs) for the two VT types associated with intrusion (left) and sagging (right).

### 4.3 Waveform-based clustering

To distinguish different families of earthquakes, we applied a waveform-based clustering technique, combining information from the waveform similarity and the differential S-P times, which reflect the distance to Mayotte. We first computed the 3-component cross-correlation at station YTMZ for each events pair, using a 12 s time window of raw waveforms starting 1 s before the P onset and bandpass filtered between 0.25 and 2.0 Hz. The cross-correlation was transformed into a distance value by mapping cross-correlation values between 1 (correlation) to -1 (anti-correlation) to distances between 0 (highest similarity) and 1 (lowest similarity). The distribution of the differential S-P times shows a clear minimum at 5.15 s, which separates two major groups of VT seismicity based on the distance to Mayotte. We attributed one group to dike propagation and the other group to sagging above the depleting reservoir (Fig. S11a). To force the separation between these two main families, we additionally fixed the distance value to 1 (i.e. dissimilar events) whenever the event pair include one VT associated with dike and one to sagging. Finally, we used a density-based seismicity clustering algorithm<sup>30</sup> to create a cluster whenever for one VT there were at least 19 others (1% of the dataset) with a distance below 0.15. Results are illustrated in Fig. S12 which shows the distance matrices, sorted chronologically and after the clustering. Since the density-based algorithm allowed for unclustered events, we finalized the process by assigning each of the unclustered VTs to one of the defined clusters, depending on its mean similarity to those in each cluster.

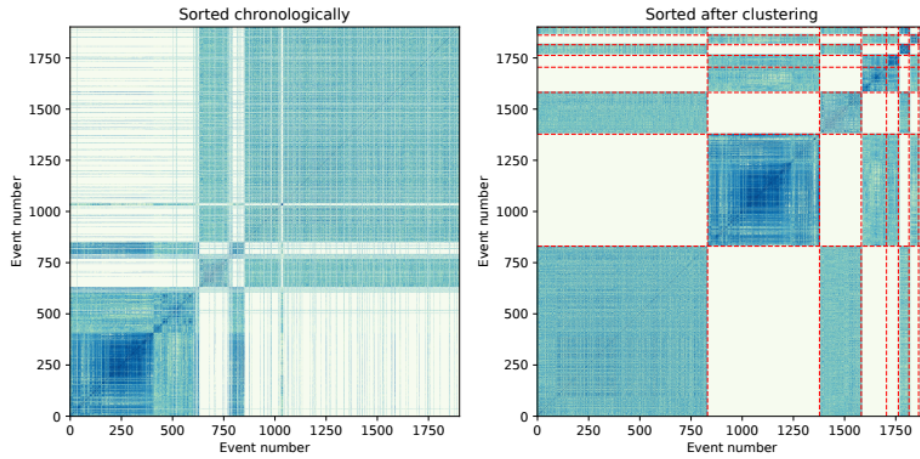


**Fig. S12 | Results of the waveform-based clustering for VT seismicity.** The similarity matrices are built using the cross-correlation of filtered 3-component raw waveforms at YTMZ and a comparison of S-P differential times, with dark blue to white colours, representing high to low similarity. The left matrix, where VTs are sorted chronologically, highlights the change from dominant dike-related VT activity to sagging-related VT activity, on August 19, 2018 (event numbers 630-631). In the right matrix, events are resorted into 8 clusters, which are plotted in different colours in Figs 2 and 3.

## 5 VLPs

### 5.1 Detection

VLPs were detected through the simultaneous identification of monochromatic seismic signals at four broadband stations at regional distances (FURI, MSEY, ABPO, and LSZ). Data were processed for the time period between 1 January 2013 and 5 March 2019. We selected 30 min time windows, starting every 2 minutes. These time series, corrected for their instrumental response, were bandpass filtered between 10 and 20 s. Using a moving window approach, amplitude spectra were first computed for each spatial component, then a mean spectra estimated and this was finally normalized. When the window contains monochromatic VLP signals, the normalized spectrum shows a clear dominant peak.

In the period preceding the seismic sequence (from 2015 until early 2018) one single VLP signal was detected: it occurred on 30 January 2018. From June onward hundreds of VLP signals were detected, showing dominant periods around 15-16 s (Fig. S13). The VLP catalogue was further enhanced following a template-matching approach. Continuous times series envelopes in the 10 - 20 s frequency band were fitted with those from the largest VLP event, which occurred on November 11, 2018. Potential new VLP detections were checked manually, picked, and either validated or rejected, by looking at their spectrograms. The checking procedure allowed for the rejection of a few false detections, mostly associated with regional earthquakes with long coda and narrow spectral content. This procedure provided a final list of 407 VLPs.

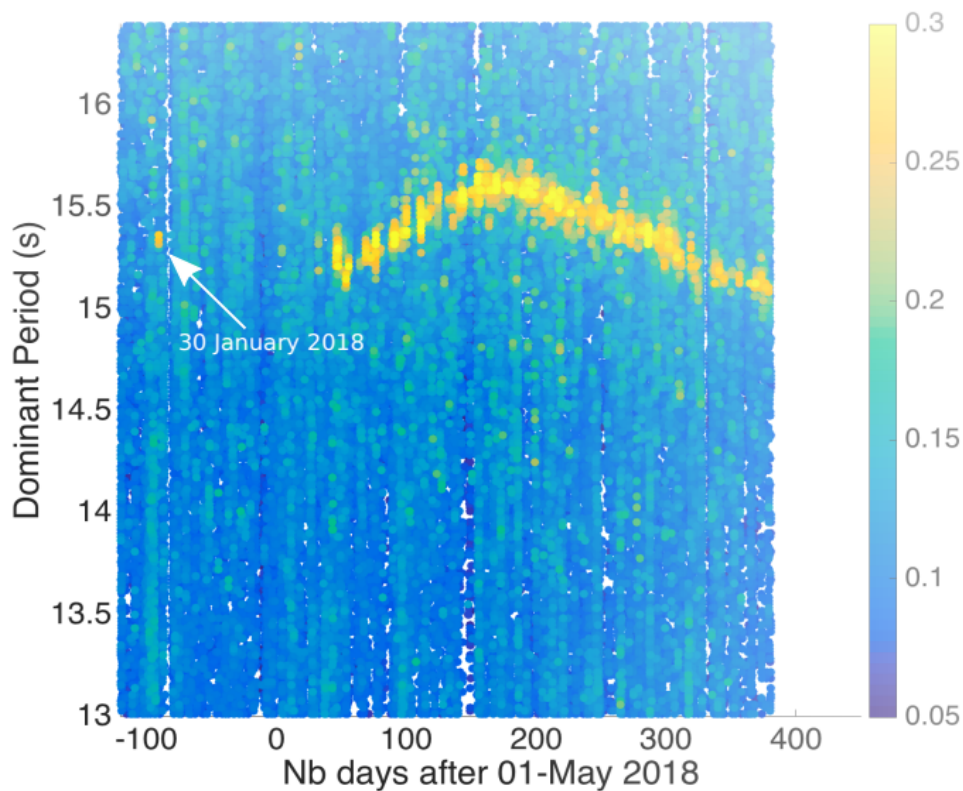


**Fig. S13 | Peak spectra and associated dominant period at ABPO station for all 30-minute-long time windows.** High peak values indicate monochromatic signals.

## 5.2 Amplitude and spectra characterization

Dominant periods of VLPs at Mayotte showed a clear, smooth variation over time (Fig. S13), starting at about 15.2 s in June 2018, increasing to 15.6 s in October 2018, and then steadily decreasing in the following months. By the end of February 2019, the dominant period was 15.3 s, close to the starting value, and later it decreased further.

A surface wave magnitude was estimated based on the following attenuation relation:

$$M_s = \log_{10}\left(\frac{A}{T}\right) + 1.66 \log_{10}(d) + 3.5 \quad (1)$$

where  $d$  is the epicentral distance from the average VLP location,  $T$  is the dominant period and  $A$  the maximum vertical displacement amplitude.

The surface wave magnitude uncertainty depends on the quality of the amplitude measurements for the considered period ( $T = 15.5$  s). The monochromatic characteristic of the VLPs allowed these amplitudes to be easily picked. The standard deviation for the  $M_s$  estimations among the 4 used seismic stations was in the order of  $\sim 0.4$  magnitude units. We computed ratios among different magnitude estimates obtained using data from different stations. A deviation from a magnitude ratio of  $\sim 1$  can be attributed to the source radiation pattern. When the ratio among magnitude estimations ( $M_s$ ) of different stations remained constant over time, the VLPs had a similar radiation pattern and the relative magnitude uncertainties were assumed to be small. The main limitation of our relative  $M_s$  estimation resulted from instrumental response problems occurring on LSZ and FURI stations. We noticed changes of the instrumental responses provided at two times during the crisis, which affected the final estimated magnitudes by less than 10%.

### 5.3 VLP source inversion

For the VLP event, the source inversion was conducted following a similar procedure as for the VT events. However, in this case, we used only the regional stations and performed the inversion in the frequency range of 0.06 - 0.07 Hz, given the monochromatic characteristic of VLP signals. In order to model the VLP oscillation, the source time function was modelled as a dampened harmonic oscillator as:

$$S(t) = \exp\left(\frac{-t}{\tau}\right) \sin(2\pi f t) \quad (2)$$

where  $f$  is the resonance frequency, and  $\tau$  is the decay time. Therefore, the inversion also inferred these two additional parameters. For overlapping VLP events, only the largest was modelled by our approach.

## 6 Deformation data analysis and modelling

On Mayotte Island, four GNSS stations showed large horizontal displacements and subsidence of up to 20 cm from 1 July 2018 to 1 April 2019. We used these GNSS data to constrain the deflation source.

### 6.1 Identification of deformation transients

We used the GNSS station MAYG to constrain the onset of the deformation signals associated with the activity off Mayotte Island; this station has the longest time series among those installed on the island. We applied simple change point analysis<sup>31-32</sup> to the GPS time series and then verified when the daily GPS measurements overcame a threshold given by the observed pre-transient sample variance. The latter check indicated when the deformation signal could be safely used for modelling the geodetic signal.



Regional linear transient deformation of Mayotte Island was calculated between 2014 and 2018. These trends were removed from the whole length of the data series (2014-2019), obtaining a time series for each of the three components with a zero mean before the onset of the transient deformation in March 2018. The East and North components show a scatter of  $\sigma \sim 3$  mm, while the vertical component shows larger scatter  $\sigma \sim 9$  mm between 2014 and 2018.

Two non-parametric change point tests were applied on the detrended time series: (1) Pettitt test<sup>31</sup> and (2) Whitney-Mann-Wilcoxon test<sup>32</sup>. The results indicate that the change point  $x_t$  is between 20 May and 2 June, 2018. Only for the North component did the Pettitt test detect a change point earlier in February). Thus, it appears that the deformation has started a couple of weeks after the onset of swarm activity off Mayotte coinciding with the upward migration of seismicity and the onset of VLP signals, which was first detected on 2 June, 2018.

The change point  $x_t$  could be used to model the deformation, but deformation values in early June were still within  $\pm\sigma$  bounds of the 2014 - 2018 transient and are statistically indistinguishable. To define the timing of the long-term change, we could also use the  $2\sigma$  rule, i.e.  $x_i > |2\sigma_{2014-2018}|$ . This criterion indicated that the deformation signal increased above  $2\sigma$  significance from 15 June (North), 9 July (East) and 15 July, 2018 (vertical) onward.

## **6.2 Deformation source modelling from GNSS surface displacements**

Based on the change point analysis we inferred the cumulative displacement on Mayotte Island, for the period of time 1 July 2018 to 1 April 2019, reported in Tab. S5. We used this cumulative displacement to model the deformation source.

**Tab. S5:** GNSS displacement rates (mm yr<sup>-1</sup>) used in the inversions, error is 1 $\sigma$ .

	E	N	Up
MAYG	200.57 $\pm$ 1.02	-4.58 $\pm$ 0.80	-149.73 $\pm$ 2.46
BDRL	212.37 $\pm$ 1.12	87.47 $\pm$ 0.87	-142.33 $\pm$ 2.61
KAWE	216.87 $\pm$ 1.23	-17.20 $\pm$ 0.92	-144.13 $\pm$ 2.51
GAMO	195.07 $\pm$ 1.02	-8.95 $\pm$ 0.77	-82.67 $\pm$ 2.56

### 6.2.1 Bayesian inference with axisymmetric point sources in a layered medium

We tested different point dislocation sources and velocity/elasticity models<sup>11, 33</sup> against the observed GNSS data and evaluated the different source models in a Bayesian inversion scheme (using the Grond<sup>11</sup> framework). Beside models P2017, P2017B and CRUST1, and in order to reflect the uncertainty of the regional layered elasticity model, we used 25 additional uniform realisations of a gradient elasticity model representing different crustal gradients and thicknesses between 15 and 30 km (Fig. S2). The results of the Bayesian inversion are shown in Fig. S14-S16.

We found that an isotropic source model in a homogeneous half-space cannot adequately represent the observations and overestimates the vertical displacements. To make use of more realistic dislocation source models, we designed a constrained MT-based point-source model. This source model represents a vertically elongated, deflating ellipsoid, similar to the point compound dislocation model<sup>34</sup> or an ellipsoidal cavity<sup>35</sup>.

The combination of an isotropic volume source model with a vertical compensated linear vector dipole (CLVD) together with perturbed gradient elasticity models provides a better physical representation of the measured surface displacements.

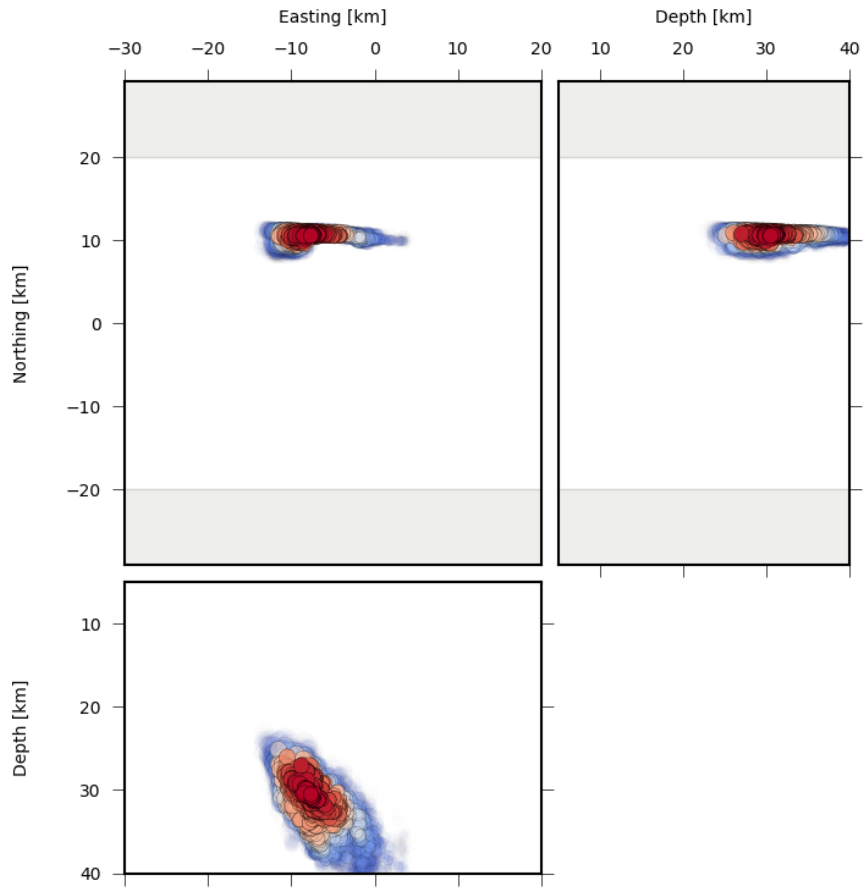


**Fig. S14 | Location plot of the ensemble of best solutions in three cross-sections.** Symbols show best volume locations, and colours indicate low (red) and high (blue) misfit. The deflating source of deformation is located  $23 \pm 3.1$  km East of Mayotte, at a depth  $32 \pm 3.5$  km. Volume change ( $\Delta V$ ) is  $1.67 \pm 0.37$  km<sup>3</sup>.

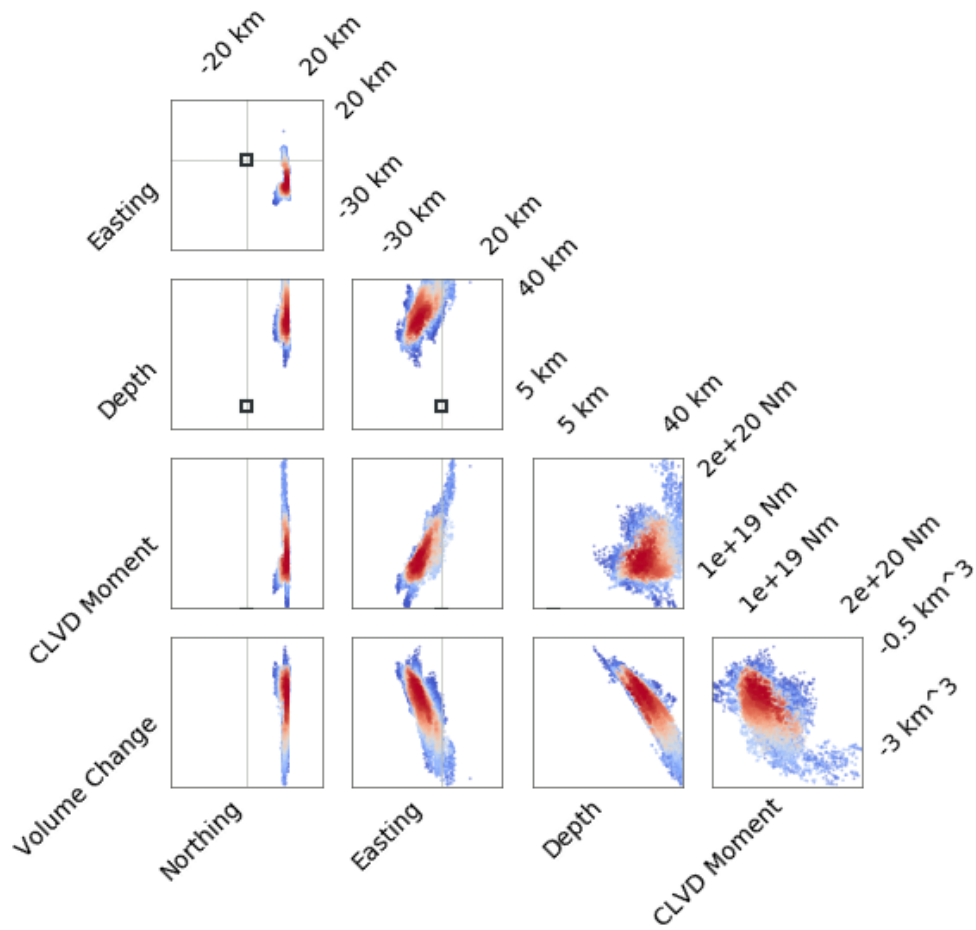


**Fig. S15 | 2D distributions of the inferred source parameters help to evaluate the resolution of source parameters and to identify parameters trade-offs.** A subset of model solutions is shown in two dimensions as points for all possible parameter pairs. Point colour indicates the misfit for the model solution with blue for high misfit models and red for low misfit models. Dark grey boxes mark the initial reference solution.

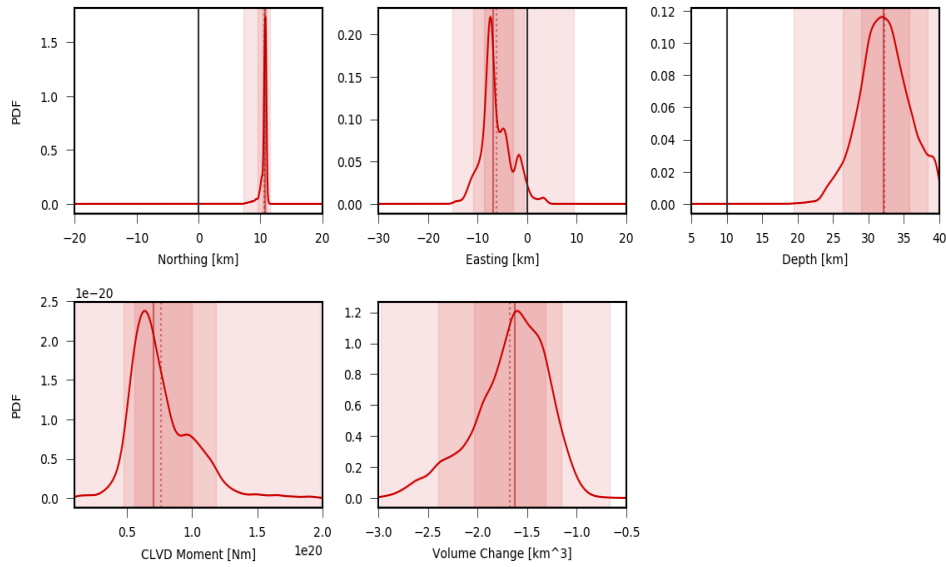


**Fig. S16 | Distribution of the problem's parameters.** The histograms are shown as Gaussian kernel densities (red curved solid line). The red solid vertical lines give the median of the distribution and the dashed red vertical line the mean value. Dark gray vertical lines show reference parameter values. The overlapping red-shaded areas show the 68% confidence intervals (innermost area), the 90% confidence intervals (middle area) and the minimum and maximum values (widest area). The plot ranges are defined by the given parameter bounds and show the searched model space.

### 6.2.2 Bayesian inference of generalised point sources in a homogeneous medium

We tested point Compound Dislocation Model<sup>34</sup> sources with a variety of constraints to remove some of the parameters: isotropic (4 parameters), horizontal dislocation (4 parameters), one vertical dislocation (5 parameters), three perpendicular dislocations (one of which horizontal, 7 parameters), three perpendicular dislocations (two of which are vertical and have the same potency, 5 parameters).

For the inversion, we use genetic algorithm optimisation<sup>36-37</sup> to find the optimal solution (minimum misfit), which we then use as the starting point in our Bayesian inference scheme. To sample the posterior pdfs we used the Delayed Rejection Adaptive Metropolis (DRAM<sup>38-39</sup>), which is an

efficient adaptive Markov Chain Monte Carlo scheme, implemented in the software package MCMCSTAT for MATLAB (<https://mjlaine.github.io/mcmcstat/>).

Results are given in Tab. S6 and Figs. S17-S21. Solutions are compared with the Akaike Information Criterion, results are 4506, 7804, 292, 680, 317 for the isotropic (Mogi), horizontal dislocation (sill), vertical dislocation (dike), vertical axisymmetric point CDM (prolate ellipsoid) and vertical triaxial point CDM (prolate ellipsoid), respectively.

**Tab. S6. Summary of inversion results.** For consistency with the other solutions, potency is declared rather than volume change (for isotropic sources, potency=volume change\*1.8).

Source type/Par.	Lower a priori	Upper a priori	Lower 99%	Upper 99%	Optimal
<b>Isotropic (Mogi)</b>					
Lon	45.2	47.8	45.633	47.494	45.694
Lat	-13.2	-12.5	-12.861	-12.535	-12.880
Depth (km)	5	200	32	160	41
Potency* (km <sup>3</sup> )	-70	0	-125	-6.5	-9.2
<b>Horizontal dislocation (sill)</b>					
Lon	45.2	47.8	45.935	46.930	46.481
Lat	-13.2	-12.5	-12.911	-12.530	-12.735
Depth (km)	5	200	49	179	100
Potency (km <sup>3</sup> )	-70	0	-70	-14	-46
<b>Vertical dislocation (dike)</b>					
Lon	45.2	45.9	45.410	45.475	45.421
Lat	-13.1	-12.6	-12.807	-12.794	-12.802
Depth (km)	5	70	18.1	23.8	20.3
Orientation (°)	0	179	167	171	169
Potency (km <sup>3</sup> )	-10	0	-1.7	-1.1	-1.3
<b>Axisym. pCDM (prol. ellipsoid)</b>					
Lon	45.2	45.9	45.460	45.604	45.484
Lat	-13.1	-12.6	-12.797	-12.772	-12.788
Depth (km)	5	70	20.3	31.5	23.2
Potency_x (km <sup>3</sup> )	-10	0	-3.2	-1.4	-1.8
Potency_y (km <sup>3</sup> )	-10	0	-3.2	-1.4	-1.8
Potency_z (km <sup>3</sup> )	-10	0	-0.34	-0.00036	<del>-9.5e-11</del>
<b>Triaxial pCMD</b>					
Lon	45.2	45.9	45.424	45.554	45.419
Lat	-13.1	-12.6	-12.806	-12.785	-12.802
Depth (km)	5	70	19.3	27	20.2
Orientation(°)	0	90	10	81	79
Potency_x (km <sup>3</sup> )	-10	0	-2.3	-6.1e-3	<del>-2.5e-5</del>
Potency_y (km <sup>3</sup> )	-10	0	-2.8	-1.2	-1.3
Potency_z (km <sup>3</sup> )	-10	0	-0.14	<del>1.5e-4</del>	<del>-6.5e-11</del>

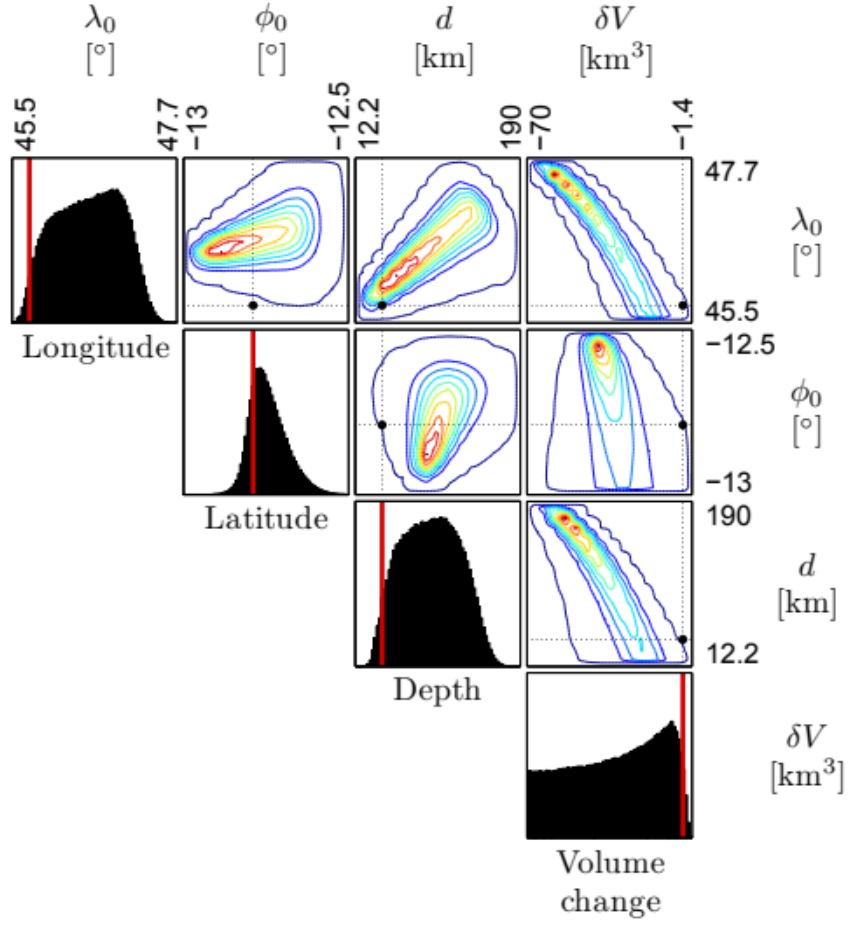


**Fig. S17 | Marginal and joint probability density functions (pdfs) of the deformation source parameters (isotropic point source).** The red bar in the marginal and the black dot in the joint distributions represent the optimal model (minimum misfit).



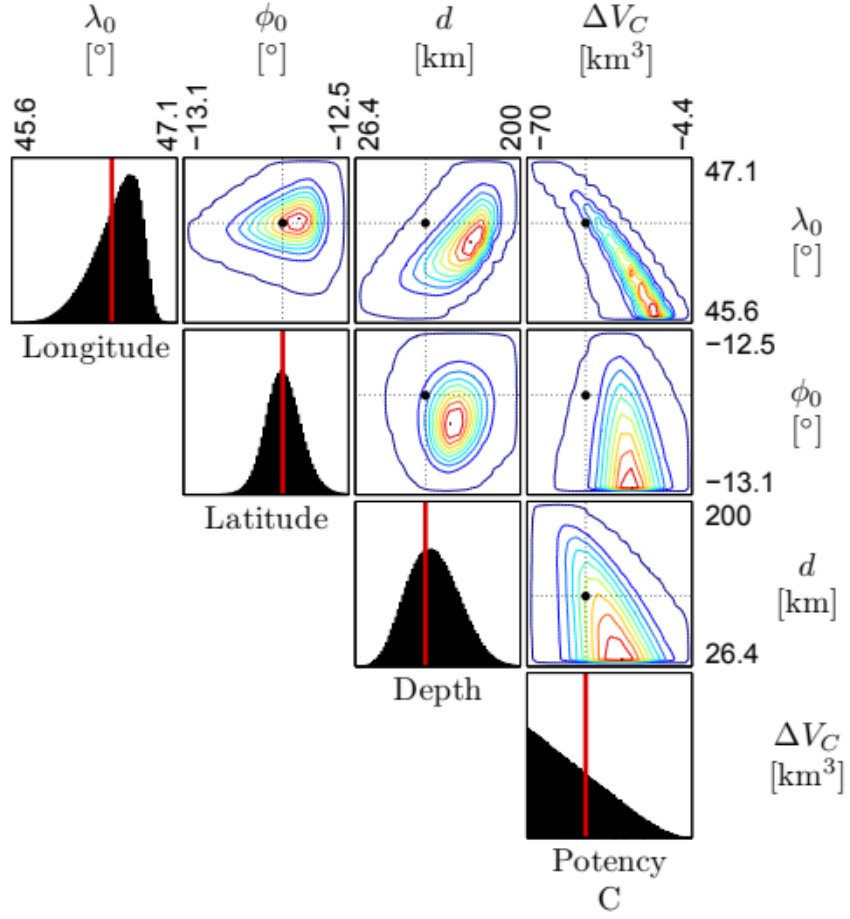


**Fig. S18 | Same as for Fig. S17, but for a horizontal tensile dislocation.**

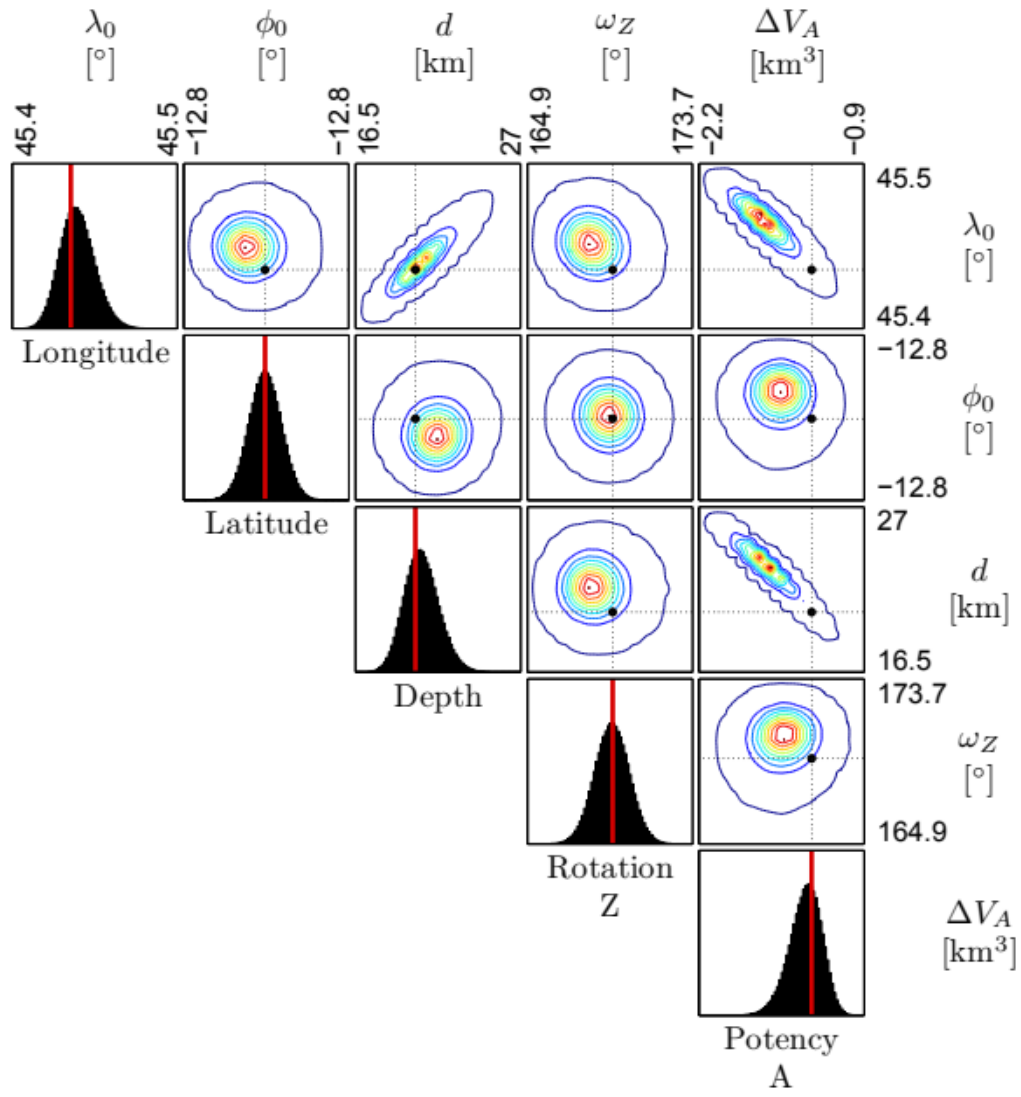


**Fig. S19 | Same as for Fig. S17, but for a vertical tensile dislocation.**

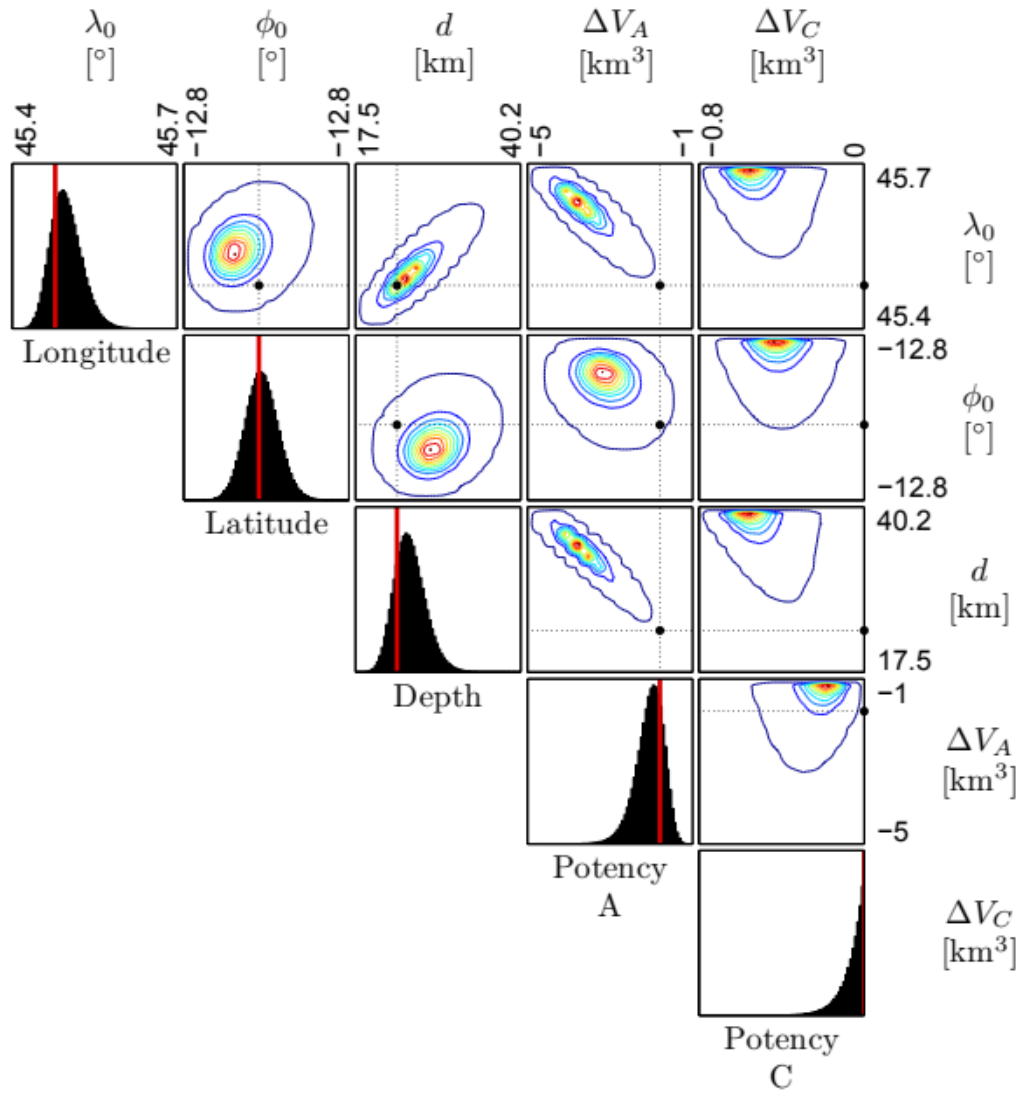


**Fig. S20** | Same as for Fig. S17, but for a vertical axisymmetric point CDM.

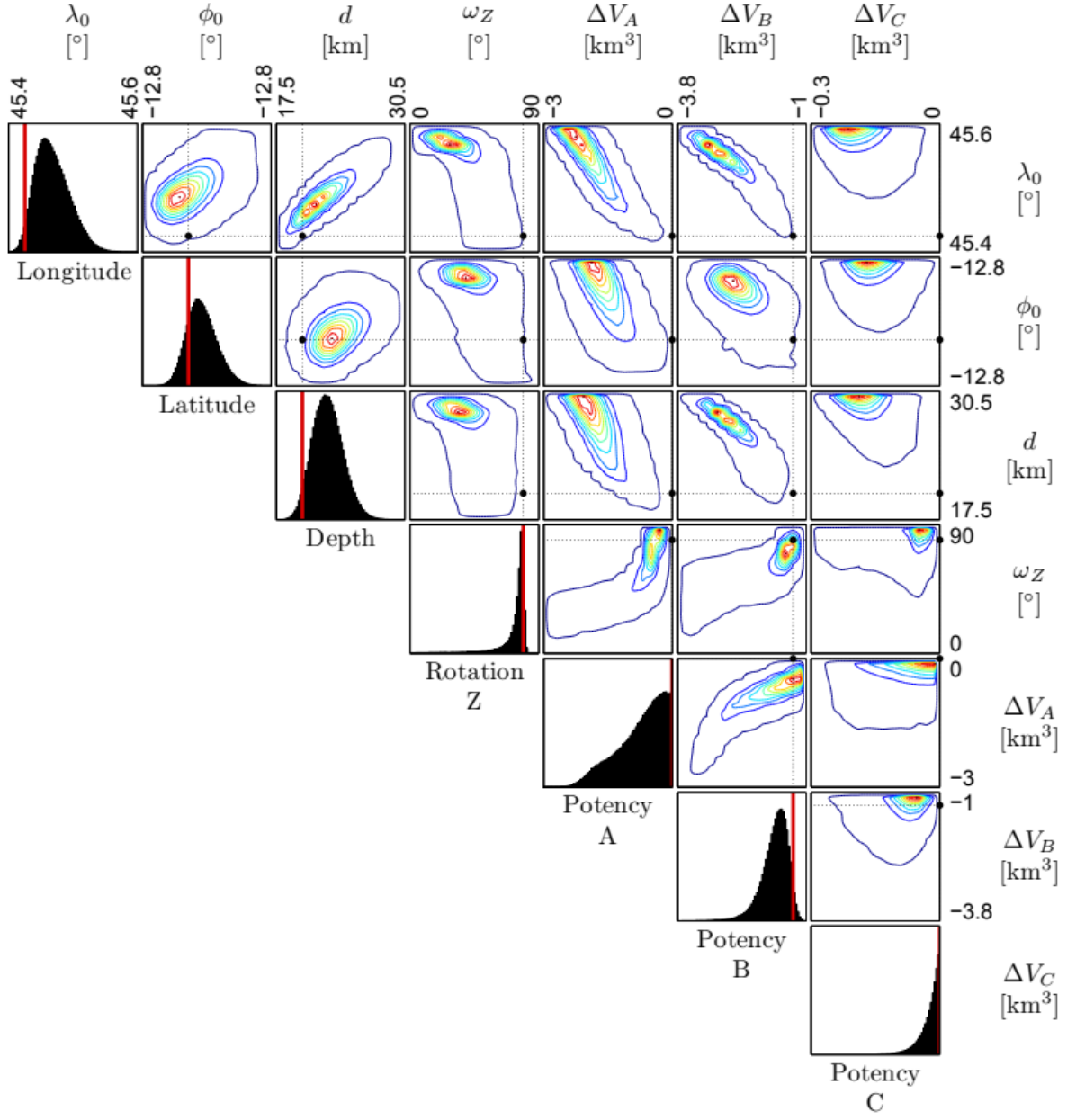


**Fig. S21 | Same as for Fig. S17, but for a vertical triaxial point CDM.**

## References

1. Cesca, S., et al. Seismic catalogues of the 2018-2019 volcano-seismic crisis offshore Mayotte, Comoro Islands, GFZ Data Services, <http://doi.org/10.5880/GFZ.2.1.2019.004> (2019)
2. Scripps Institution of Oceanography. IRIS/IDA Seismic Network. International Federation of Digital Seismograph Networks. Dataset/Seismic Network. <https://doi.org/10.7914/SN/I> (1986)
3. Albuquerque Seismological Laboratory (ASL)/USGS. Global Seismograph Network (GSN - IRIS/USGS). International Federation of Digital Seismograph Networks. Dataset/Seismic Network. <https://doi.org/10.7914/SN/IU> (1988)
4. GEOFON Data Centre. GEOFON Seismic Network. Deutsches GeoForschungsZentrum GFZ. <https://doi.org/10.14470/tr560404>. (1993)
5. Institut De Physique Du Globe De Paris (IPGP), & Ecole Et Observatoire Des Sciences De La Terre De Strasbourg (EOST). GEOSCOPE, French Global Network of broad band seismic stations. Institut de Physique du Globe de Paris (IPGP). <https://doi.org/10.18715/geoscope.g> (1982)
6. Blewitt, G. et al. Harnessing the gps data explosion for interdisciplinary science. *Eos*, **99**, 4872–4886 (2018).
7. Petersen, G. M. et al., M. Automated quality control for large seismic networks: Implementation and application to the AlpArray seismic network. *Seismol. Res. Lett.* **90**, 1177–1190 (2019).
8. Rueda, J. and Mezcua, J. (2015). Orientation Analysis of the Spanish Broadband National Network Using Rayleigh-Wave Polarization. *Seismol. Res. Lett.*, **86(3)**, 929–940 (2015).
9. Stachnik, J. C., et al., Determination of New Zealand Ocean Bottom Seismometer Orientation via Rayleigh-Wave Polarization. *Seismol. Res. Lett.*, **83(4)**, 704–713 (2012).
10. Heimann, S. et al., Pyrocko - An open-source seismology toolbox and library. V. 0.3. GFZ Data Services. <http://doi.org/10.5880/GFZ.2.1.2017.001> (2017)

11. Heimann, S., et al., A Python framework for efficient use of pre-computed Green's functions in seismological and other physical forward and inverse source problems. *Solid Earth Discussions*, <https://doi.org/10.5194/se-2019-85> (2017)
12. Nougier, J. et al. The Comoros Archipelago in the western Indian Ocean: volcanology geochronology and geodynamic setting. *J. Afr. Earth Sci.* **5**, 135–145 (1986).
13. Michon, L. The volcanism of the Comoros archipelago integrated at a regional scale. In *Active Volcanoes of the Southwest Indian Ocean* (eds Bachelery, P., Lénat, J.-F., Di Muro, A. & Michon, L.) 233–244 (Springer-Verlag, 2016).
14. Heimann, S. et al. Grond - a probabilistic earthquake source inversion framework. V. 1.0. GFZ Data Services, <http://pyrocko.org/grond/docs/current/> (2018).
15. Pratt, M. et al. Shear-velocity structure of the crust and upper mantle of madagascar derived from surface wave tomography. *Earth Planet. Sci. Lett.* **458**, 405–417 (2017).
16. Laske, G. et al. Update on CRUST1.0 - A 1-degree Global Model of Earth's Crust, *Geophys. Res. Abstracts*, **15**, Abstract EGU2013-2658 (2013).
17. Bassin, C. et al. The current limits of resolution for surface wave tomography in north america. *AGU 81*, F897, <http://igppweb.ucsd.edu/~gabi/rem.html> (2000).
18. Heyburn, R., et al. How deep was the Dudley (UK) earthquake of 22 September 2002?, *Journal of seismology*, **9(1)**, 61-71 (2005).
19. Heyburn, R. & Fox, B., Multi-objective analysis of body and surface waves from the Market Rasen (UK) earthquake. *Geophys. J. Int.*, **181**, 532–544. (2010).
20. Letort, J., et al., Multiobjective Optimization of Regional and Teleseismic Data to Constrain the Source of the 12 September 2016 Mw 5.4 Earthquake in South Korea. *Bull. Seismol. Soc. Am.* (2017).
21. Lemoine, A. et al. The volcano-tectonic crisis of 2018 east of Mayotte, Comoros islands. *EarthArXiv*, DOI: 10.31223/osf.io/d46xj (2019).

22. Letort, J. et al., Lateral variations of the guerrero-oaxaca subduction zone (Mexico) derived from weak seismicity (mb 3.5+) detected on a single array at teleseismic distance. *Geophys. J. Int.*, **213**, 1002–1012 (2018).
23. Engdahl, E.R., van der Hilst, R. & Buland, R. Global teleseismic earthquake relocation with improved travel times and procedures for depth determination, *Bull. seism. Soc. Am.*, **88**, 722–743 (1998).
24. Bondár, I., & D. Storchak, Improved location procedures at the International Seismological Centre, *Geophys. J. Int.*, **186**, 1220-1244, doi: 10.1111/j.1365-246X.2011.05107.x (2011).
25. Letort, J., et al., A new, improved and fully automatic method for teleseismic depth estimation of moderate earthquakes ( $4.5 < M < 5.5$ ): application to the Guerrero subduction zone (Mexico). *Geophys. J. Int.*, **201**, 1834-184.8 (2015).
26. Craig, T. J., Accurate Depth Determination for Moderate Magnitude Earthquakes Using Global Teleseismic Data. *Journal of Geophysical Research: Solid Earth*, **124**(2), 1759-1780 (2019).
27. Florez, M. A., & Prieto, G. A., Precise Relative Earthquake Depth Determination Using Array Processing Techniques. *Journal of Geophysical Research: Solid Earth* (2017).
28. Montalbetti, J. F., & Kanasewich, E. R. Enhancement of Teleseismic Body Phases with a Polarization Filter, *Geophys. J. Int.*, <https://doi.org/10.1111/j.1365-246X.1970.tb01771.x> (1970).
29. Beyreuther, M., et al. ObsPy: A Python Toolbox for Seismology, *Seismol. Res. Lett.*, **81**(3), 530-533, DOI: 10.1785/gssrl.81.3.530 (2010)
30. Cesca, S. et al. Seismicity monitoring by cluster analysis of moment tensors. *Geophys. J. Int.* **196**, 1813–1826 (2014).
31. Pettitt, A. A non-parametric approach to the change-point problem. *J. Royal Stat. Soc. Ser. C* , **28**, 126–135 (1979).
32. Mann, H. B. & Whitney, D. R. On a test of whether one of two random variables is stochastically larger than the other. *The annals mathematical statistics* 50–60 (1947).

33. Wang, R., et al. PSGRN / PSCMP a new code for calculating co- and post-seismic deformation, geoid and gravity changes based on the viscoelastic-gravitational dislocation theory, *Computers and Geosciences*, **32**, 527–541 (2006).
34. Nikkhoo, M. et al. Compound dislocation models (CDMs) for volcano deformation analyses. *Geophys. J. Int.*, ggw427, DOI: 10.1093/gji/ggw427 (2017).
35. Segall, P. *Earthquake and volcano deformation* (Princeton University Press, 2010).
36. Holland, J. H. *Adaptation in Natural and Artificial Systems*. Ann Arbor: University of Michigan Press (1975).
37. Haupt, R.L. & Haupt, S. E., *Practical Genetic Algorithms*, JOHN WILEY & SONS, INC., Hoboken, New Jersey, 2nd edition (2004).
38. Haario, H., et al. An adaptive Metropolis algorithm, *Bernoulli*, **7**, 223-242. doi: 10.2307/3318737 (2001)
39. Haario, H., et al. DRAM: Efficient adaptive MCMC, *Statistics and Computing*, **16**, 339-354. doi: 10.1007/s11222-006-9438-0 (2006)